UiT The Arctic University of Norway

Faculty of Science and Technology

Department of Physics and Technology

Wind at Northern Senja

Use of numerical weather prediction models for wind resource assessment

Gjøran Emil Hansen

Master's thesis in Energy, Climate and Environment

EOM 3901

December 2020

Abstract

Wind resource assessment for establishing decentralized power production in remote and complex areas is challenging due to a lack of observational data. Numerical Weather Prediction (NWP) models can be used to provide data where no observations exist. This thesis uses NWP models to do a wind resource assessment at northern Senja. The power grid in the area is prone to voltage drops, and decentralized power production would release some transmission capacity. The study is twofold: The first part investigated the model performance at three observation sites Hekkingen, Innhesten, and Senjahopen. The second part is a wind resource assessment based on model data.

Calculated statistical scores and wind roses showed that Arome 500 with a horizontal resolution of 0.5 km was the best model for predicting wind speed and direction in the fjords at northern Senja. Furthermore, no evident correlation between Arome 500, AROME-Arctic and NORA3 could be concluded from the statistical scores and wind roses, mainly due to short overlapping periods and datasets. Production estimates at Mykjeneset, Giskhaugen, and Sporra were computed from three Enercon wind turbines' power curves. Two levels of turbulence corrections were applied. Before any turbulence corrections; Sporra showed the highest annual energy production of 2587 MWh and a capacity factor of 36.8% for the Enercon E-53 turbine. After the turbulence corrections, the same turbine had the highest annual energy output at Giskhaugen of 2180 Mwh and a capacity factor of 31%.

Acknowledgements

At first, I would like to thank my supervisor Eirik Mikael Samuelsen and co-supervisor Yngve Birkleund for many constructive discussions and guidance.

I would also like to thank my family for the endless support throughout my time as a student at UiT. I would especially like to thank my mother and father, Anne-Sissel and Realf Hansen, who have always encouraged me in reaching my full potential.

At last, I would like to thank my dear Vilde for supporting me in everything I do.

Contents

Acronyms

SL	Semi-Lagrangian
TKE	Turbulent kinetic energy
MASL	Meter above sea level
HA	HARMONIE-AROME
LAM	Limited area model
SW	Short-wave
LW	Long-wave
SIC	Sea-ice concentration
SST	Sea-surface temperature
LSM	Large-scale mixing
LBC	Lateral boundary conditions
MAGL	Meter above ground level
MBE	Mean bias error
MAE	Mean absolute error
RMSE	Root mean squared error

Chapter 1

Introduction

1.1 Background

A 66 kV network cable from Finnsnes to Silsand supplies Senja with power from the mainland. The installed hydropower on the island can provide up to 15.7 MW extra power during periods with heavy load. Furthermore, 22 kV grid lines distribute the power on the northern parts over long distances. As a result, the endpoints are prone to voltage drops during heavy loads. Recent years, the industry, especially seafood industry on Husøy and at Senjahopen have expanded, and so has the need for stable power supply. During periods with heavy load, the power delivered by the 66 kV power line and the hydropower plants is not sufficient. An unstable and insufficient power supply could have critical consequences both for the industry and for the local community.

An update of the existing grid is expensive as well as time consuming. A low-cost alternative compared to updating the existing grid are decentralized power production. Energy production and storage in the neighbouring area to the biggest power consumers would lead to less load on the power lines and hence a more stable power supply. Decentralized energy production from renewable energy sources such as wind, therefore, might be a part of the complex solution to the power supply problem at Northern Senja.

1.2 Former research

Observational data from meteorological stations are frequently used in most wind resource assessments today such as in [1],[2], and [3]. At least a year of data is needed in order to capture the yearly variations in wind speed and direction[4]. Most meteorological stations are centralized and in remote areas, the amount of observational data available is limited. As a first assessment of the wind energy potential at remote

locations for possible decentralized power production, numerical weather prediction (NWP) models are frequently used[5]. Dependent on the computational power, the models could provide historical measurements over a long period of time. The accuracy of the models could be good for the given area providing sufficient results as a first wind energy assessment for areas where no observations exists[6].

Processes occurring on scales smaller than the horizontal scale of the model is called sub-grid processes. These processes has to be parametrized in the models[7]. Different models provide different choices of schemes which are used to parametrize the sub-scale processes such as; turbulence, cloud micro-physics, and radiation[7].

The Topography in complex terrain in coastal areas of Northern Norway are characterized by steep mountains and narrow fjords. The orography are here mostly unresolved and wind patterns which are characteristic for the complex terrain are, therefore, mostly unresolved as well. This results in errors in the modelled wind field[8]. A higher-resolution model is needed in order to resolve the complex terrain flow, and to obtain more accurate wind power assessments[9].

1.3 Scope of the study

The biggest power consumers at northern Senja are located in the neighbouring area around Senjahopen and Husøy. Wind power production from a location close to these may increase the transmission capacity. The terrain on northern Senja, especially close to Senjahopen and Husøy, are complex with steep mountains separated with narrow fjords. Observations from a single observation site only provide information from a point in the terrain. Due to the complex topography in the area, wind direction and speed cannot be assumed to be the same at other similar locations.

Model data from numerical weather prediction NWP models could provide th necessary data for areas where no observations exists. However, the quality of the models is dependent on model performance for the area. The model set-up are in this thesis presented, and the models performances are evaluated statistically and visually against observations from the three observation sites; Hekkingen, Innhesten, and Senjahopen. The aim of the model verification is to find a relation between the Arome 500 model with a horizontal resolution of 0.5 km which only stretches a year, to the NORA3 model with a horizontal resolution of 3 km. These models only overlap 6 months, and the AROME-Arctic model is, therefore used due to a year of overlap with both.

Furthermore, model data will be used for creating wind-resource maps over northern Senja. Possible locations for wind energy production are presented on the basis of the resource maps. The locations are then described in more detail, and power production estimates are calculated, and evaluated at least for a year dependent on the findings from the model verification.

1.4 Outline of the thesis

The thesis is divided into the following 4 chapters excluding the introduction:

- **Chapter 2** provides the relevant theory used in the thesis.
- **Chapter 3** presents the methodology by describing the model and observation data as well as statistical scores and parameters, selection of turbines, and power corrections.
- **Chapter 4** presents and discusses the results from the comparison between model and observational datasets and presents and discusses the wind resource assessment.
- **Chapter** 5 will conclude the results and provide some topics for further work

Chapter 2

Theory

2.1 Equation of motion

The equation of motion describes the momentum of a a fluid due to internal and imposed forces. In certain forms, the momentum equations are referred to as the Euler equations or the Navier-Stokes equations dependent on whether the viscosity of the fluid is neglected or not, respectively[10]. The mathematics describing these equations are expressed by considering an infinitesimal control volume. Two reference frames are commonly used, one is the Eulerian frame of reference and the other is the Lagrangian. In the Eulerian reference system, the control volume is spatially fixed. Fluxes of air through the boundaries of the volume would change the mass, momentum, and energy budget. In the Lagrangian reference system, the infinitesimal control volume follows the motion of the fluid and the number of particles in the volume are held fixed[11].

The material derivative also called the substantive derivative describes the rate of change of an element vector or scalar moving with a infinitesimal control volume with velocity $\boldsymbol{v}$ with respect to time[10]. The material derivative of a vector $\boldsymbol{b}$, scalar variable b, and an integral of a vector or a scalar variable k is expressed in [10] as follows:

$$\frac{D\boldsymbol{b}}{Dt} = \underbrace{\frac{\partial \boldsymbol{b}}{\partial t}}_{\text{I}} + \underbrace{(\boldsymbol{v} \cdot \nabla)\boldsymbol{b}}_{\text{II}} \tag{2.1}$$

$$\frac{Db}{Dt} = \underbrace{\frac{\partial b}{\partial t}}_{\text{I}} + \underbrace{(\boldsymbol{v} \cdot \nabla b)}_{\text{II}} \tag{2.2}$$

$$\frac{D}{Dt}\int_V \rho k dV = \int_V \rho \frac{Dk}{Dt} dV \tag{2.3}$$

where $\nabla = \left(\boldsymbol{i}\frac{\partial}{\partial x}, \boldsymbol{j}\frac{\partial}{\partial y}, \boldsymbol{k}\frac{\partial}{\partial z}\right)$, $\frac{\partial}{\partial t}$ is the partial derivative with respect to time, and V is the volume of the control volume. I and II in Equation (2.1) and (2.2) is the local rate

of change and the advection term, respectively. The momentum of a particle is given by the mass m multiplied by the three dimensional velocity vector $\boldsymbol{v}$. The momentum per unit volume is, therefore, described as $\rho\boldsymbol{v}$ where ρ is the density of the air. Forces acting on the control volume V are from newtons second law and Equation (2.3):

$$\int_V \rho \frac{D\boldsymbol{v}}{Dt} = \int_V \boldsymbol{F} dV \tag{2.4}$$

where $\boldsymbol{F}$ is the forces per unit volume. The integrand vanishes since the volume is arbitrary and we get the following expression for how fluid accelerates if subject to forces:

$$\frac{\partial \boldsymbol{v}}{\partial t} + (\boldsymbol{v} \cdot \nabla) = \frac{1}{\rho}\boldsymbol{F} \tag{2.5}$$

For a fluid element in a rotating coordinate system such as the atmosphere. The equation of motion or the Navier Stokes equation can be written on vector form as:

$$\underbrace{\frac{D\boldsymbol{v}}{Dt}}_{\text{I}} = \underbrace{-(\boldsymbol{f} \times \boldsymbol{v})}_{\text{II}} \underbrace{-\frac{1}{\rho}\nabla p}_{\text{III}} + \underbrace{\boldsymbol{F}}_{\text{IV}} + \underbrace{\boldsymbol{g}}_{\text{V}} \tag{2.6}$$

where I is the accelleration terms, II is the Coriolis terms, III is the pressure gradient terms, IV is the friction terms and V is the gravitational term.

2.2 Numerical weather prediction

Numerical weather prediction (NWP) is a fundamental component of weather forecasting today. The atmosphere is treated as an initial value problem. Future weather is predicted by integrating non-linear, partial differential equations such as the momentum equations, whereas the initial value is the observed weather as proposed by Abbe[12] and Bjerknes[13] in the beginning of the 1900s.

Three main steps are fundamental in the process of running the meteorological model; discretization of the atmosphere, initialization of the model field, and calculation of the evolution of atmospheric variables. The atmospheric variables are continuous in time and space. In order to solve the governing equations numerically, the earth surface have to be discretized[14]. Furthermore, the model has to be initialized. For operational limited area models (LAM) and global models, available observations are optimally fitted to the model in a process called data assimilation[15]. LAM can also be initialized without observations and a data assimilation process. Then global models such as ERA-5 from the European Centre for Medium-Range Forecasts (ECMWF) are used as the model initial field. As the model is initialized, the calculation process begins by solving the initial value problems and calculating the evolution of the atmospheric variables into the future[16].

2.2.1 Discretization

The atmospheric variables are as already mentioned continuous in time and space, and in order to solve the evolution of atmospheric variables, discretization of the atmosphere is necessary. The discretization of the atmosphere is explained by first considering the horizontal discretization, and then the vertical. Most models today uses a grid point method where the area of interest are divided into a number of grid points[17]. Different gridded horizontal coordinate systems are used today. A commonly used grid for global models is the reduced Gaussian grid. The number of longitudinal grid points along a latitude is then constant and specified where the number of grid points on a latitude varies such that the distance between the grid points, dx, are approximately the same [18]. For global models such as ERA-5 the reduced Gaussian horizontal grid cover the earth surface with singularities at the poles. For LAM, rectangular grids are most often used with equally distanced grid points. An illustration of an rectangular grid for the LAM AROME-Arctic over northern Senja can be seen in Figure 2.1.

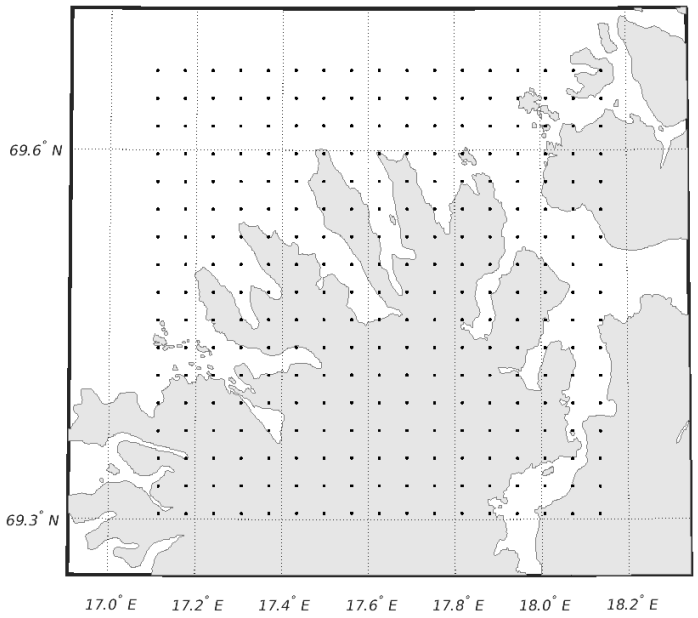

Figure 2.1: An example of a rectangular grid with grid points marked as black dots. The horizontal resolution is approximately dx = 2.5 km with 17×17 grid points over Northern Senja.

The vertical is discretized into different layers. Most models today uses a pressure based vertical coordinate such as the σ-coordinate defined first in [19] or the η-coordinate defined in [20]. Common for the pressure-based coordinate systems are that the lowest layer follows the terrain, and when moving higher up in the atmosphere, the layers flattens out. Due to a rapidly decreasing vertical pressure gradient in the atmosphere the density of the layers are highest near the surface. An example of the pressure based coordinate systems are shown in Figure 2.2.

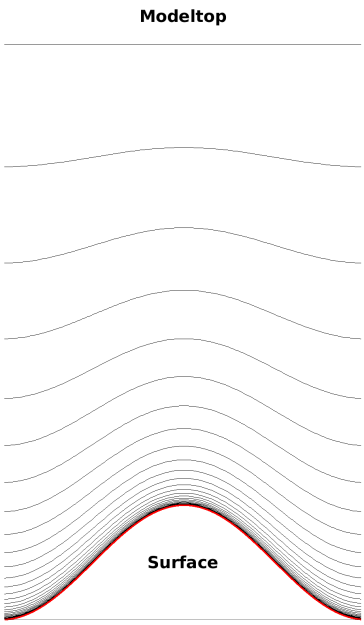

Figure 2.2: An example of the vertical discretization with 30 vertical layers over an hill in the terrain where the red line is the surface. The density of the layers are highest close to the surface and decreases as moving up into the atmosphere.

2.2.2 Model initialization

The model begins with an initial state called analysis. The initial field for a global model such as ERA-5 are obtained from a mixing between an earlier forecast and observations in a process called data assimilation or data analysis. The data assimilation step is crucial for global models in order to obtain as accurate model results as possible. For LAM, the initial field could be obtained from a data assimilation process such as for the global models, or obtained directly from the global model.

In the data assimilation process, observations from several sources are used, whereas the most important are satellite observations[21]. The observations can be of varying quality and registered at different locations at different times. Feeding observational data directly into the model would result in non-physical and poor model results[16]. Observations are, therefore, preprocessed before the assimilation step in a so called screening process involving several steps such as spatial thinning of observational data, and background checks i.e. checks of observations against a old forecast[15][22].

Furthermore, the basic principle of the assimilation step is to obtain an initial state vector of the atmosphere which is a selection of the best elements, i.e. blending between observations and the old forecast, in order to minimize the errors of the initial

conditions fed into the model. This is done by minimizing an objective function or a cost function[15].

2.2.3 Evolution of variables

As the atmosphere's initial state is fed into the model, the model can start to calculate how the variables will evolve in time and space. A widely used technique which are used for computing the evolution of the prognostic variable's are the Semi-Lagrangian (SL) method. The method can be explained by considering a flow in one spatial dimension x. From a Lagrangian reference system, the one dimensional tracer field $\xi(x,t)$ where $Q(x,t)$ represents sinks and sources of the tracer field where x is the position in x direction, and t is the time. The evolution of ξ may be described as in [23]:

$$\frac{d}{dt}\xi(x,t) = Q(x,t) \tag{2.7}$$

Furthermore, the velocity u of the parcel is from the definition of velocity:

$$\frac{d}{dt}x = u \tag{2.8}$$

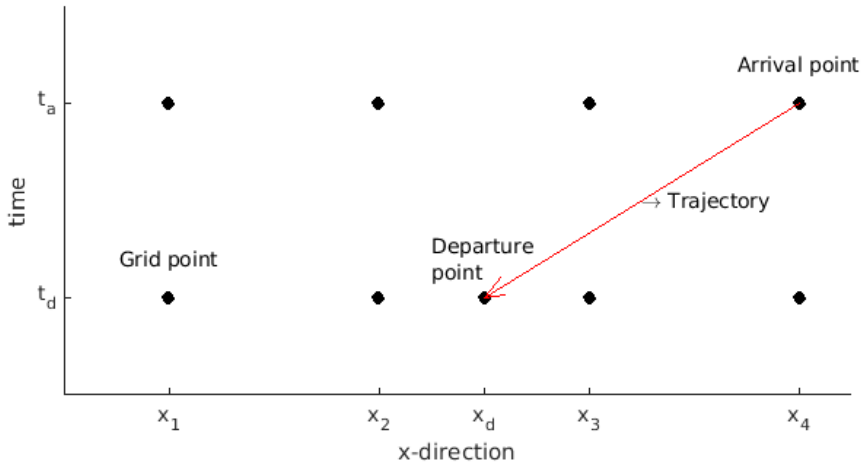

Figure 2.3: The 2D graphical representation of the semi-Lagrangian method, where the x-axis represents the spatial dimension, and the y-axis represent the time dimension. The solid black circles represent the grid points. The solid red line represents the trajectory that needs to be calculated from the arrival point to the departure point.

The semi-Lagrangian approach of calculating the trajectories is that at any time step $t + \Delta t$, a parcel coincides with a specific grid point as illustrated in Figure 2.3, i.e. the arrival point. The trajectory is calculated from the known arrival point of the parcel to the unknown departure point as is represented by the solid red line in Figure 2.3. By integrating Equation (2.7) we get:

$$\frac{\phi_a - \phi_d}{\Delta t} = \frac{1}{2}\left[Q_a + Q_d\right] \tag{2.9}$$

where ϕ is the numerical appriximation to ξ, a denotes the arrival point, and d denotes departure point [23]. In order to compute the value of the field at the departure point, the trajectory back to the departure point has to be computed from Equation (2.8):

$$\frac{dx}{dt} = u(x,t) \Rightarrow r_a - r_d = \int_{t_d}^{t_a = t_d + \Delta t} u(x,t')dt' \tag{2.10}$$

where r_a is the arrival grid point, r_d is the unknown departure point, t_d is the time when the parcel left the departure point, and $t_a = t_d + \Delta t$ is the arrival time at the grid point [24]. The velocity integral need to be solved numerically. This is often done by using the mid point rule and we get:

$$r_a - r_d = \Delta t u \left(\frac{r_a - r_d}{2}, t_d + \frac{\Delta t}{2} \right) \tag{2.11}$$

However, from the mid point rule, another problem arises from knowing the trajectory midpoint $t_d + \frac{\Delta t}{2}$. A second order time extrapolation formula is used before interpolation of the extrapolated velocity field at the estimated mid point $u^{t_d + \Delta t/2}$[24]. Furthermore, a fixed point algorithm is used to compute the position of the departure point[24].

The last step of the semi-Lagrangian method after the departure point is found is to interpolate the value of the surrounding grid points to the departure point. This is done in order to obtain the value of Q_d and ϕ_d at the departure point[24].

2.3 Wind power

The power in the wind is an essential topic considering wind power generation, and especially siting. The kinetic energy of air molecules in motion can be expressed as follows:

$$E_k = \frac{1}{2} m v^2 \tag{2.12}$$

where m is the mass and v is the wind . Power in the wind can be expressed as the derivative of kinetic energy with respec to time:

$$P = \frac{dE}{dt} = \frac{1}{2} \dot{m} v^2 \tag{2.13}$$

The mass flow rate $\dot{m}$ can be expressed as:

$$\dot{m} = \rho A v \tag{2.14}$$

where ρ is the density of the air and A is the swept area of the turbine blades. Substituting Equation (2.14) into (2.13) and we get:

$$P_w = \frac{1}{2} \rho A v^3 \tag{2.15}$$

As is evident from Equation (2.15) is that the power in the wind varies as a cube of the wind speed. Small fluctuations in the wind speed would, therefore, generate large

fluctuations in the power. Since $A \propto P_w$, the larger the rotor, the more power would be generated. Furthermore, the density of air is defined from the ideal gas law as:

$$\rho = \frac{p}{RT} \tag{2.16}$$

where p is the pressure, T is the temperature in Kelvin, and R is the gas constant of air. The humidity may be considered by replacing RT with $R_d T_v$ where R_d is the gas constant for dry air and T_v is the virtual temperature. Equation (2.16) then become:

$$\rho = \frac{p}{R_d T_v} \tag{2.17}$$

where the virtual temperature can be calculated as follows:

$$T_v \approx T(1 + 0.61q) \tag{2.18}$$

where q is the specific humidity in g/kg. From Equation (2.15), one can observe that the density is proportional to the power in the wind. From Equation (2.17), one can see that the air density is inverse proportional to the humidity and temperature of the air. At Northern latitudes, fluctuations in power production could be significant due to large variations in temperature and humidity, e.g. in the winter with low temperatures and less water content in the air, more power could be generated[25].

The manufacturer gives the power extracted from the wind turbine at different wind speeds. When plotting the output power P_o as a function of wind speed v, we obtain the power curve. An illustration of a power curve is shown in Figure 2.4. A wind turbine has a cut-in wind speed that is the weakest wind needed to generate power. Furthermore, dependent on the generator, there is a maximum limit of how much it could generate. This limit is the rated power of the turbine. The threshold wind speed, in which the rated power is generated, is known as the rated wind speed. Wind speeds above this threshold would not generate more power as is evident from the figure. The cut-out wind speed is the strongest wind the turbine will operate under, i.e. for wind speeds above the cut-out threshold the turbine blades would pitch or stall depending on wind power regulation the turbine uses. A pitch controlled turbine uses an active control system that varies the blade angles, hence reduces the lift force and, therefore, the rotational speed. A stall regulated wind turbine has turbine blades formed such that when the wind speed increases above a specific value, the lift force and the rotational speed decreases. The cut-out wind speed limit is set in order to prevent damage on the wind turbine.

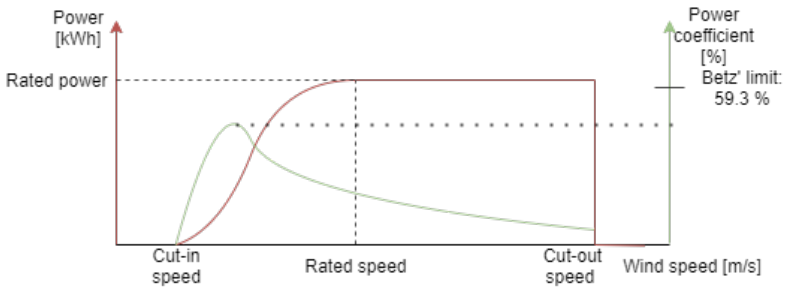

Figure 2.4: The red line represents an example of a power curve for a wind turbine, whereas the green line represents the efficiency of the same turbine. Cut-in, rated, and cut-out speed as well as rated power are illustrated.

The power coefficient of a wind turbine is the ratio of Power output from the wind turbine to the power in the wind. The power coefficient Cp is given as:

$$Cp = \frac{P_o}{P_w} \tag{2.19}$$

where P_o is the power output. The maximum power the turbine can extract from the wind is 59.3 % and is known as the Betz' limit[26]. If a turbine extracted 100% of the energy from the wind, the velocity downstream would be zero, i.e. no wind behind the turbine. However, the power extracted by a wind turbine rarely reach this limit due to e.g. electrical losses. Furthermore, assumptions done in deriving the Betz' limit are; idealized rotor with infinitely many blades as well as infinitely thin blades, no rotor drag, no hub and turbine tower and no turbulence in the stream. These assumptions do not coincide with real atmospheric flow, hence the power coefficient of wind turbines never reaches the Betz' limit [26].

Another measure on the performance of a wind turbine is the capacity factor CF:

$$CF = \frac{E_o}{E_{\text{max}O}} \tag{2.20}$$

where $E_{\text{max}O}$ is the maximum energy a turbine could produce over a period t, and E_o is the actual energy output in that period. The average capacity factor was 35% in the USA in 2018[27].

2.4 Turbulence

Turbulence can be defined as fluctuations or irregularities in the air. It can be seen as swirls in the fluid or so-called eddies which is superimposed to the mean flow[28]. Turbulence can arise of several reasons whereas the two primary reasons are; high wind shear, and buoyancy[28]. A high wind shear arises due to frictional drag. The surface friction causes a high wind shear near the surface to develop resulting in generation of turbulence. Mountains and obstacles such as buildings and threes amplify this by deflecting the flow and generating wakes on the obstacle's downwind side and adjacent to it. Buoyant turbulence arises due to density differences between warm and cold air. As warm air is less dense than cold air, warm air rises and cold air sinks resulting in vertical motions and mixing between horizontal fluid layers[28].

The horizontal turbulence intensity is the standard measure of turbulence used in the wind industry. A measure of the turbulence intensity which also include the vertical fluctuations in the wind is the turbulent kinetic energy (TKE) which is defined in [28] as follows:

$$\frac{TKE}{m} = \overline{e} = \frac{1}{2}\left(\overline{u'}^2 + \overline{v'}^2 + \overline{w'}^2\right) \tag{2.21}$$

where u', v', and w' is the horizontal and vertical wind fluctuations, respectively[28].

The turbine, the blades' structure, and the control system are designed to extract the maximum power from the wind between the cut-in wind speed and the rated

wind speed. At speeds beyond the rated wind speed, the pitch control, or stall control ensures that the excess wind power is deflected. Gusty and turbulent winds causes rapid changes in the wind speed and direction hence sudden changes in load on the turbine that could cause damage[29]. Turbulence could also reduce or enhance the power output from a wind turbine. The reduction is especially evident at wind speeds close to, and above, the rated power of the turbine, whereas the increased output are seen for speeds close to the cut-in wind speed[30][31]. Therefore, it is important to quantify the turbulence at the location to give more accurate power prediction- and cost estimates. In areas with complex topography, such quantifications are even more important due to potentially more mechanical turbulence.

2.5 Complex terrain flow

The area around northern Senja has complex topography with steep mountains and narrow fjords as earlier mentioned. Regional wind patterns are disturbed in complex terrain by mechanical forcing from the topography and by thermal forcing generating local winds which emerge from thermal fluxes[32]. Common for both categories is that they vary largely both spatially and temporally. Wind-power siting have been restricted to less complex areas characterized by high mean wind speed. However, the complex terrain may enhance the mean wind speed for a given area due to local specific flow[32]. Downslope windstorms and gap winds are characteristic for complex terrain and may enhance the mean wind speed for an area.

Gap wind

Gap winds are strong local winds confined in a fjord or a valley. Weber and Kafmann found in [33] that the gap winds arises mainly due to orographic modification of the large scale flow in narrow fjords and valleys. However, gap winds can also arise from synoptic-scale pressure gradients, i.e. a low pressure on one side of the gap, and a high pressure on the other side of the gap[34]. For both cases, a pressure gradient across the gap arises, resulting in an acceleration of wind through the gap. For narrow fjords and valleys such as on northern Senja, the pressure gradient; thus, the wind will follow the axis of the lowest level in the gap[34].

Downslope windstorm

Strong and severe gusty winds down the lee slope of mountains are called downslope windstorms. Flow over a mountain is dependent on several factors; the wind speed and direction, shape and height of the mountain, and the stability of the atmosphere. If wind manages to flow over the mountain in a stably stratified layer, mountain waves are formed. If the mountain waves become very steep and brakes, e.g. due to a decrease in wind speed with height such as a 180° change in wind direction, a

turbulent region is created above the mountain. The turbulent region reflects the energy resulting in strong winds plunging underneath thus generation of downslope windstorms[35].

Chapter 3

Data and methods

3.1 Site, time and observations

Observations are obtained from three different locations on the Senja island; Hekkingen, Senjahopen, and Innhesten. An overview of the observation sites are shown in Figure 3.1. The exact positions of the observation sites are listed in Table 3.1. The northernmost part of Senja is characterized by deep fjords and high mountains, whereas the highest mountain, Breitinden, is ranging 1001 meters above sea level (masl). Details regarding the observation sites such as surrounding topography, and data from these are described in further detail in Section 3.1.1-3.1.3.

Location	**Latitude**	**Longitude**	**mamsl**
Hekkingen	69.60° N	17.83° E	33
Senjahopen	69.50° N	17.51° E	5
Innhesten	69.42° N	17.58° E	912

Table 3.1: Location of the observation sites from where observational data sets are obtained.

3.1.1 Hekkingen

Hekkingen is a small island located north-east of Senja as shown in Figure 3.1. Observations are obtained from the mast situated 33 masl at the north-west tip of the island. The surrounding area is relatively open where the highest neighbouring mountain is Kampen 654 masl in the west direction and Astritinden 742 masl in the south direction. Both of these are 6 km away from the observation site. The closest mountain in the east direction is Kvitfjell 566 masl 11 km away. An anemometer MI250 measures wind direction and speed with 10-minute intervals. The anemometer is located 10 magl. Measurements of temperature are obtained from a thermometer 2 magl. The dataset is granted by The Norwegian Meteorological Institute (MET). It

Figure 3.1: Map of Northern Senja with north up. Red points marked with 1, 2, and 3 representing the locations of the observation sites at Hekkingen, Senjahopen, and Innhesten, respectively (NVE.no).

has hourly wind- and temperature measurements from 1 January 2002 to 1 October 2020. Some observations were missing due to factors such as icing and maintenance. Direction and wind speed was of bad quality before 15 September 2015. The dataset is therefore shortened to the period from 15 September 2015 to 1 October 2020. After applying corrections for bad data, 97.2% of hourly data could be made available for further analysis.

3.1.2 Senjahopen

Senjahopen is the name of the observation site owned by Statens Vegvesen near the village Senjahopen. Its located in the innermost part of the north-west south-east oriented Mefjorden which is only 2.6 km wide at the station's location (see Figure 3.1). Mountains ranging up to 811 masl are surrounding the site in the north and east direction. In the south, mountains range up to 750 masl, as shown in Figure 3.1. The anemometer at the station measures wind speed and direction every 10 minutes. The data set is granted by Statens Vegvesen. The observations span the period from 27 February 2015 to 28 December 2019. After preparing the data, 58.6%

of the observations were found to be of acceptable quality.

3.1.3 Innhesten

Innhesten is a mountain ranging 916 masl. The Norwegian Armed Forces granted data from this location. Complex topography is surrounding the mountain, as shown in Figure 3.1. Steep slopes are close to the observation site, and high neighbouring mountains ranging above Innhesten are present in all directions, e.g. Istindan in south, Stormoa in west, and Breitinden in the north-east. The Innhesten dataset span the period from 4 January 2003 to 1 October 2020. Before 1 January 2019, very few observations were obtained. Therefore, the dataset is shortened to span the period from 12 July 2019 to 1 October 2020. After preparations of the data, 90.1% were of acceptable quality.

3.2 Model data

In order to do a wind resource assessment at northern Senja, model data are used. The three models used are; Arome 500, AROME-Arctic, and NORA3. These models are based upon the model physics from HARMONIE-AROME (HA). HA is a convection-permitting numerical limited area model (LAM). The set-up and scripting system of the LAM HA involves several physical processes such as parametrization, and data assimilation[36]. Since, e.g. the set-up, initialization and boundary conditions differs between NORA3, Arome 500, and AROME-Arctic, each one is described separately in Section 3.2.4-3.2.6.

3.2.1 Model-grid

The model uses the mass-based hybrid terrain-following coordinate system η. A benefit of this vertical discretization is that the grid follows the terrain close to the ground. At intermediate levels, the effect of orography is smaller, and as a result, the layers flattens out. The layers' thickness varies from a high density of layers in the lower part of the atmosphere to lower density towards the model top. The η layers in which the atmosphere are divided into are defined in [20] as follows:

$$\eta = \frac{p}{p_s} + \left(\frac{p}{p_{s0}} - 1\right)\left(\frac{p}{p_{s0}} - \frac{p}{p_0}\right) \tag{3.1}$$

where p_0 is the defined pressure at the model top which is constant, p_{s0} is the surface reference pressure[1]. η varies monotonically from 0 at the model top to 1 at the surface

[1]The surface reference pressure is continuous in time but not in space since it follows the topography.

($0 \leq \eta \leq 1$ if $p_0 > \frac{1}{2}\max(p_s)$).

Furthermore, the model uses a horizontal Arakawa-Lamb A grid. The A-grid is illustrated in Figure 3.2. The horizontal velocity and the scalar velocities are represented at the same location as the grid-point. In the vertical, prognostic variables such as u, v, and T are defined at the full levels from $K = 1, 2, ..., \mathrm{N_{LEV}}$ where $\mathrm{N_{LEV}}$ is the total number of full levels in the model. Values of, e.g. pressure and vertical component of velocity $\dot{\eta}$ is defined at the so-called half levels which are intermediate layers between two full levels and is therefore shifted relative to the full levels. The reason for the shifted representation of the vertical is a result of derivations by the finite difference method. The number of half levels is, therefore, one less than the number of full levels ($\mathrm{N_{LEV}} - 1$)[20].

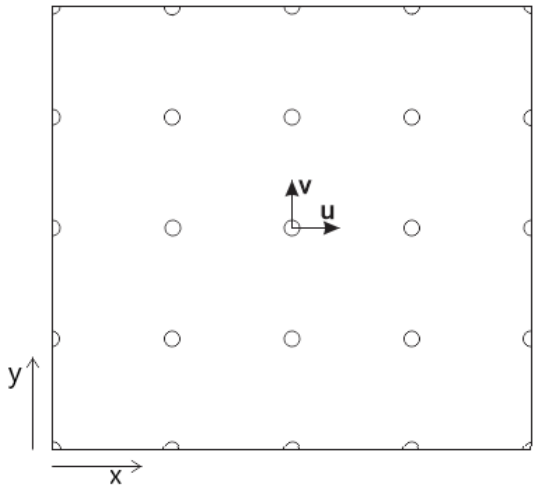

Figure 3.2: Arakawa lamb A-grid. The hollow black circles represent a grid point whereas u and v are the x and y velocity components. The scalar velocities are presented in all grid points but only illustrated in one in the figure.

3.2.2 Model-dynamics

HA is based upon the non-hydrostatic, fully compressible Euler Equation system[36]. Trajectories are calculated using a semi-Lagrangian (SL) advection scheme and a Semi-Implicit (SI) two-time-level scheme. The SI-method is performed with a scheme named SETTLS. This method treats linear and non-linear variables separately in the trajectory calculations providing better model stability[36]. Twelve prognostic variables are used: zonal wind, meridional wind, temperature, specific water vapour content, rain, snow, graupel, cloud droplets, ice crystals, turbulent kinetic energy, and the non-hydrostatic variables that are related to pressure and vertical momentum, respectively[37].

Model results from global models such as ERA-5 or IFS-HRES from ECMWF are often used as the initial and boundary conditions. The outermost boundaries are

often overspecified. Typically, an 8 point wide relaxation zone is adopted along the border of the domain. This is done in order to ensure model stability. The horizontal and upper boundary coupling is performed using the known Davies method and is implemented with the Davies relaxation scheme[36]. More details regarding the Davies Relaxation scheme can be found in [38].

3.2.3 Model-physics

The model cannot resolve the atmosphere's processes on spatial scales smaller than the distance between the grid-points, dx. Even though these processes occur on small spatial scales, they play a role in the large scale processes and, therefore, have to be considered by the model. Sub-scale processes, e.g. shallow convection, and radiation, are, therefore, parametrized in the model. The parametrization choices available in the HA physics package is described in the following section.

Radiation

The radiation scheme which is used in HA for shortwave (SW) radiation is the Morcrette scheme from ECMWF. The scheme contains six spectral intervals from 0.185 to 4.0 μm. Furthermore, for long-wave (LW) radiation, the Rapid Radiative Transfer Model (RRTM) is used where the LW radiation is divided into 16 spectral bins between 3.33 to 1000 μm[36].

The cloud cover is assumed homogeneous inside a grid box. The cloud cover value at the different η-layers in the grid box is computed by finding the maximum cloud cover value for a set of neighbouring layers. The cloud content for the overlap between cloudy layers and layers with no cloud content are set by a random overlap[39]. SW flux transfer for a cloudy sky and SW clear sky flux transfer are calculated using a delta-Eddington approximation formulated in [40] and the SW parameterization formulated in [41], respectively. The flux transfer calculations, both SW and LW, use the optical properties from the IFS radiation scheme[36].

Micro-physics

HA uses the microphysics scheme named ICE3 do describe the microphysics of warm clouds, atmospheric ice, and sub-grid condensation. Three solid hydrometors are included, namely; ice crystals, snow, and a combination of hail and graupel[36]. Further description of the ICE3 scheme can be found in [42]. The horizontal advection of the hydrometors are calculated in the SL scheme whereas the vertical advection are taken care of by a separate scheme described in more detail in [43].

Turbulence

The turbulence scheme represented in HA is the HARMONIE with RACMO Turbulence (HARATU). The scheme is based on a prognostic turbulent kinetic energy equation combined with a diagnostic length scale. The diagnostic length scale is dependent on the atmospheric stability, and the calculations of length scales differ between stable conditions and near-neutral and convective conditions. The HARATU scheme is described in more detail in [36], and [44].

Convection

For non-hydrostatic LAM such as HA, deep convection, i.e. turbulent vertical motion starting from the lower atmosphere and rises above 500hPa, is expected to be resolved by the model's non-hydrostatic dynamics. The deep convection, therefore, has no parametrization in HA. Shallow convection, i.e. turbulent vertical motion where the lifting is capped below 500 hPa, still needs to be parametrized. HA uses a combined eddy diffusivity mass-flux scheme for parametrizing the shallow convection (EDMFm). The EDMFm scheme is described in more detail in [45] and [46].

Surface

The surface physics in HA is taken care of by the SURFEX scheme. The scheme is composed of several models for four main categories of surface tiles. The four main categories of surface tiles are; land surface, urbanized areas, lakes, and ocean. Each grid box are assigned one or more surface tiles. The surface fluxes are then calculated before the grid box's total flux is calculated by adding the individual fluxes of each tile weighted by their respective fractions. Further detail of the SURFEX scheme are described in [47]. The physiography of the land-cover is based on different versions of ECOCLIMAP[36]. Furthermore, several options for the surface topography can be used. The Global Multi-resolution Terrain Elevation Data (GMTED2010) is one, and gtopo30 is another.

3.2.4 AROME-Arcitc

AROME-Arctic (AA) is an operational weather forecasting model based on the HA version 40, cycle 1.1. The model produce a 66-hour forecast every 3 hours with start at 00 UTC[2] as shown in Figure 3.6. The surface variables are assimilated through the CANARI spatial interpolation tool. Sea-ice concentration (SIC) and sea-surface temperature (SST) are obtained from ECMWF through CANARI. Upper-air initial conditions are a spectral blending of the last 6 hours from the old cycle a well as an upper air data assimilation. The upper air assimilation is done with the 3DVar

[2]A forecast is produced at 00, 03, 06, 09, 12, 15, 18, 21 UTC.

scheme. The scheme is configured with 3-hour cycles as a sequential three-dimensional variational data assimilation[3]. Also, the background field for large scale mixing (LSM) is blended with the ECMWF Integrated Forecasting System High-Resolution model (IFS-HRES) forecast. the lateral boundary conditions (LBC) are obtained from IFS-HRES.

The horizontal resolution of the model is dx = 2.5 km and the vertical is divided into 65 η-layers, whereas the lowest layer is approximately 12 meters above ground level (magl). The domain of the model covers the mainland of Norway, Svalbard and large sea areas in the Arctic (see Figure 3.3a). The extracted data are a domain with similar horizontal and vertical resolution as the operational version covering northern Senja from 1 January 2019 to 11 September 2020, as seen in Figure 3.3b. Data are bi-linearly interpolated from the original domain to the domain over Northern Senja using the fimex library[4]. The data is extracted from the 00 UTC forecast from +7 hours to +30 hours. The prognostic variables extracted are wind 10, 20, 80 and 120 magl, wind gusts 10 magl, and temperature and relative humidity 2 magl. The data are granted by MET Norway.

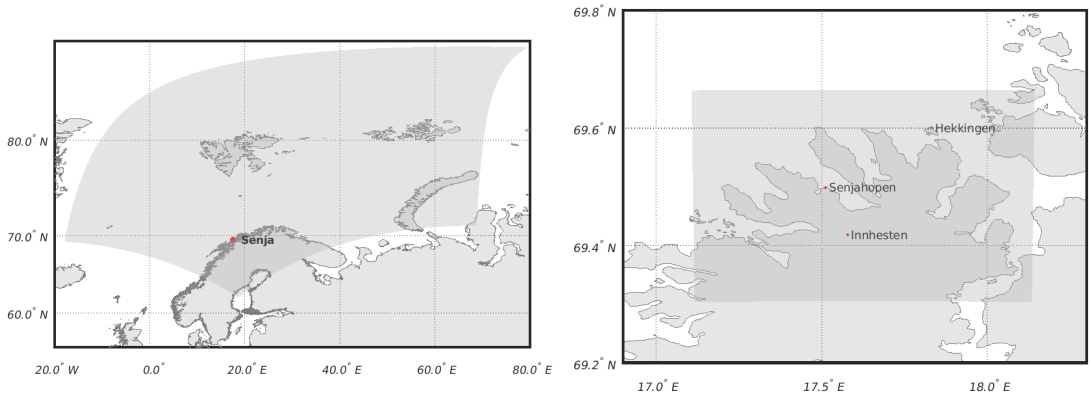

(a) AROME-Arctic domain.

(b) Extracted domain.

Figure 3.3: AROME-Arcitc domain.

3.2.5 Arome 500

The Arome 500 model is a high-resolution model executed with the HA experimental version 43, cycle 2.1. The model have been initialized for two periods. The first was from 12 July 2019 to 31 December 2019, and the second was from 1 January 2020 to 9 September 2020. Both periods are initialized with a cold start, i.e. boundary and initial conditions are obtained solely from IFS-HRES, and snow cover (SC) data are

[3]The assimilation step is performed at 00, 03, 06, 09, 12, 15, 18, 21 UTC.

[4]Fimex is a library used for manipulation and extraction of gridded data, e.g. meteorological data from models [48].

obtained from AA. The prognosis runs from 00 UTC to +36 h, as shown in Figure 3.6. Shorter prognosis are produced every 6 h at 00, 06, 12, and 18 UTC. CANARI then updates SST and SIC. The warm start initial conditions for the long prognosis at 00 UTC is obtained from the 18 UTC + 6 h shorter prognosis. Furthermore, the upper air initial conditions are obtained from a spectral mixing between the IFS-HRES boundaries and the shorter prognosis. Lateral boundaries are from IFS-HRES. An 8 point wide relaxation zone is adopted to the boundaries in order to assure model stability.

The domain of the model is shown in Figure 3.4. The models horizontal resolution is dx = 0.5 km. In the vertical, the model is divided into 90 σ-layers, whereas the lowest layer is approximately 4.5 magl. This thesis's extracted data are from 00 UTC + 7 h to +30 h, as shown in Figure 3.6. This extraction window is chosen in order to avoid spin up as the model starts. The extracted data are wind 10, 20, 50, 100 and 250 magl, wind gusts 10 magl, temperature and relative humidity 2 magl. In addition, scalar wind speed, TKE, specific humidity and temperature are extracted from σ-layer number 86. The height of this layer are approximately 48 magl. The model is executed for the SmartSenja project, by Eirik Mikal Samuelsen, MET Norway and UiT.

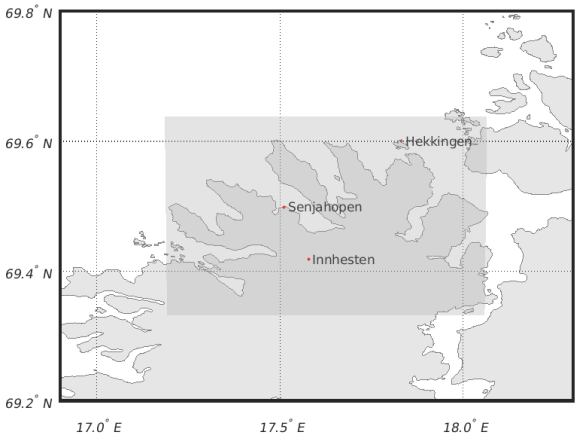

Figure 3.4: Domain of Arome 500.

3.2.6 NORA3

NORA3 is a reanalysis based on the HA model version 40 cycle 1.2. Reanalysis data from 1 January 2002 to 28 December 2019 are obtained from a downscaling of the ERA-5 reanalysis from ECMWF. Data are granted by the MET Norway project WINDSURFER/NORA3. The model was executed with 9 hour forecasts every 6 hours, i.e. model start to run at 00, 06, 12 and 18 UTC, as is shown in Figure 3.6. Every forecasting cycle uses the previous forecast as its initial field, and the boundaries are forced with ERA-5. The model have a horizontal resolution of dx = 3.0 km and

covers the mainland of Norway as well as nearby sea areas (see Figure 3.5a). The vertical is divided into 65 σ-layers whereas the lowest is at 12 magl. Data from the model is extracted with Fimex over a smaller domain with dx = 2.5 km covering Northern Senja as can be seen in Figure 3.5b. The data is extracted from +4 to +9 hours at 00, 06, 12, and 18 UTC, respectively, as shown in Figure 3.6. Wind speed and direction are extracted 10, 20, 50, 100, 250 magl, wind gust 10 magl, and relative humidity and temperature 2 magl.

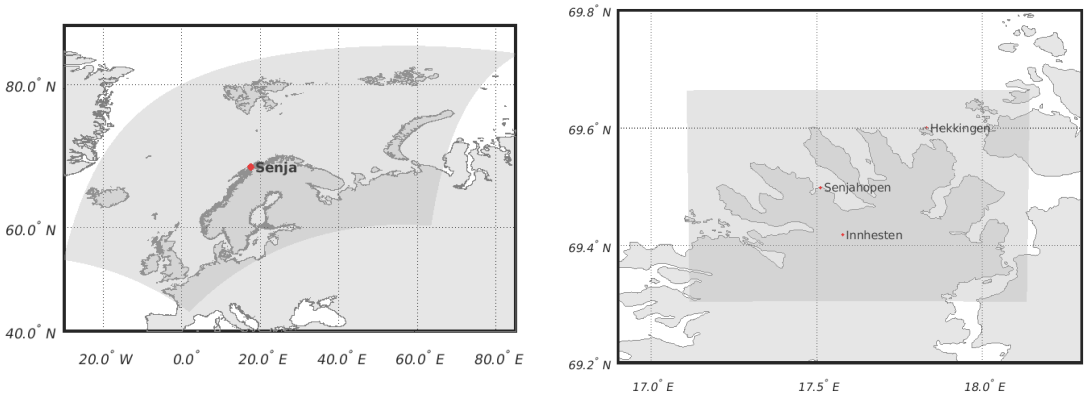

(a) NORA3 Domain.

(b) Extracted domain.

Figure 3.5: NORA3 domain.

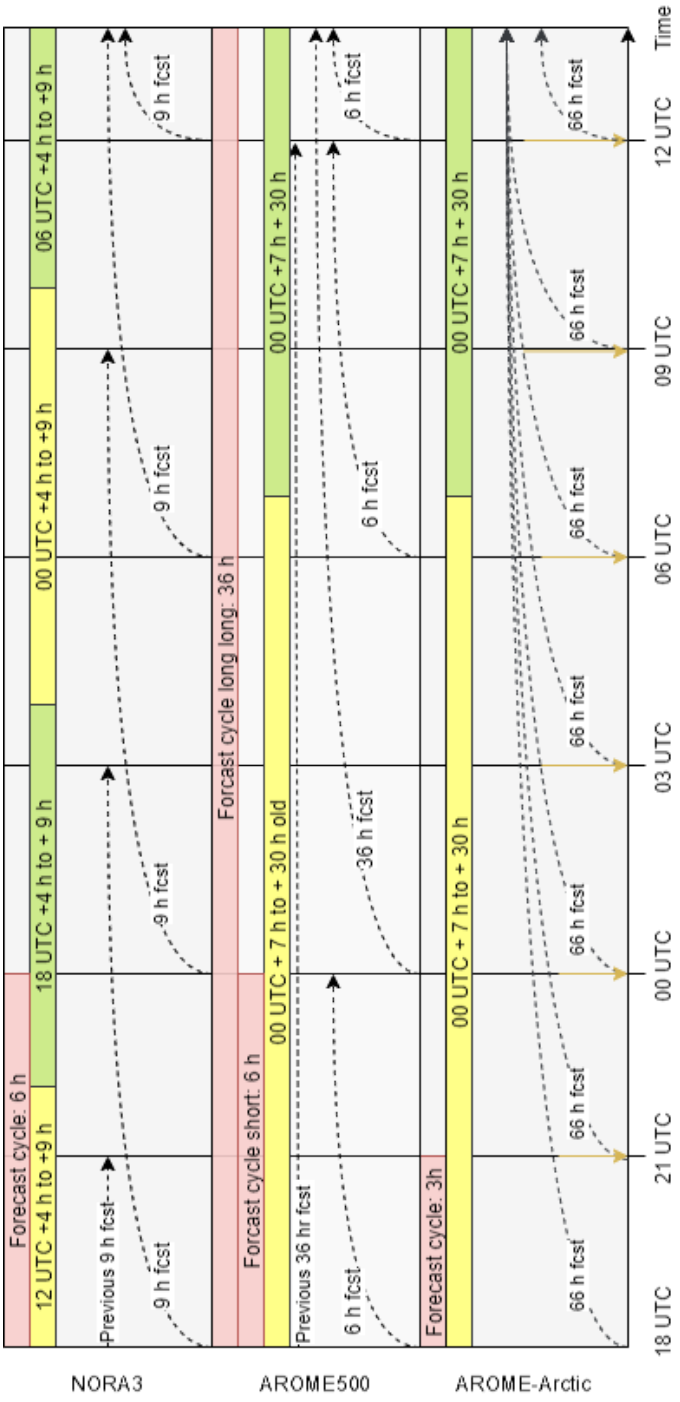

Figure 3.6: The diagram show the model cycles for NORA3, Arome 500, and AROME-Arctic. Red colours represent the forcast cycles. Arome 500 have four forecast cycles per day, 3 short, and 1 long. AROME-Arctic is the only model running the data assimilation step illustrated by yellow arrows in the figure. The yellow and green boxes represents when the data are obtained from, e.g for Arome 500 the green box represents that the data from the 00 UTC forecast is extracted +7 hours after the model run and 30 hours into the future.

3.3 Statistical methods

3.3.1 Statistical parameters

The fundamental statistical parameters are formulated by using a sample vector $\mathbf{x} = [x_1, x_2, ...x_N]$ where N indicates the number of elements in the vector. The i-th element of the vector is subscripted as x_i. The sample mean ($\overline{x}$) of the sample vector can be expressed as:

$$\overline{x} = \frac{1}{N}\sum_{i=1}^{N} x_i \tag{3.2}$$

The sample variance (σ^2) is expressed as follows:

$$\sigma^2 = \frac{1}{N-1}\sum_{i=1}^{N} (x_i - \overline{x}) \tag{3.3}$$

The sample standard deviation, σ, is the square root of the sample variance $\left(\sigma = \sqrt{\sigma^2}\right)$ [49].

3.3.2 Statistical scores

Statistical scores are used in order to estimate how the forecasted values from the models correspond with the observations. The model forecasted values and the observations can be written as two vectors $F = [F_1, F_2, ..., F_n]$ and $O = [O_1, O_2, ..., O_n]$, respectively. The mean bias error (MBE) can be expressed as:

$$MBE = \frac{1}{N}\sum_{i=1}^{N}(F_i - O_i) \tag{3.4}$$

The Bias indicates the averaged over-or underestimation between the model forecasted values and the observations. A positive bias indicates that the model overestimates, e.g. the wind speed compared to the observations on average. On the other hand, a negative value would indicate that the model forecasted values are below the observations on average. Large errors could compensate, i.e. large negative errors compensate for large positive errors resulting in a small bias. The mean absolute error (MAE) is also computed to overcome the issue of compensating errors. The MAE can be expressed as follows[50]:

$$MAE = \frac{1}{N}\sum_{i=1}^{N} |F_i - O_i| \tag{3.5}$$

In order to quantify the number of larger errors between the predicted values and observations, the the root mean square error (RMSE) was computed. The RMSE can

be expressed as follows:

$$RMSE = \sqrt{\left(\frac{1}{N}\sum_{i=1}^{N}(F_i - O_i)^2\right)} \tag{3.6}$$

The correlation coefficient is a good measure of the linear relation between two datasets and can be expressed as:

$$\rho = \frac{\sum_{i=1}^{N}(F_i - \overline{F})(O_i - \overline{O})}{\sqrt{\sum_{i=1}^{N}(F_i - \overline{F})^2}\sqrt{\sum_{i=1}^{N}(O_i - \overline{O})^2}} \tag{3.7}$$

The correlation coefficient varies from -1 to 1, whereas a exact linear correlation is 1, no correlation is 0, and negative linear correlation is -1[49].

3.3.3 Wind rose

Comparing wind direction between observations and forecasted values from the models is made visually by using wind roses. A wind rose is a polar histogram visualizing wind direction, wind speed, and data amount in each direction. The wind directions are divided into 36 directional bins, whereas each directional bins represent 10°. An example of a wind rose is shown in Figure 3.7. From the figure one can see that winds from the south-east are dominant with about 500 observations. From the colour one can observe that most winds from this direction represents the weaker winds, i.e. below 10 m/s.

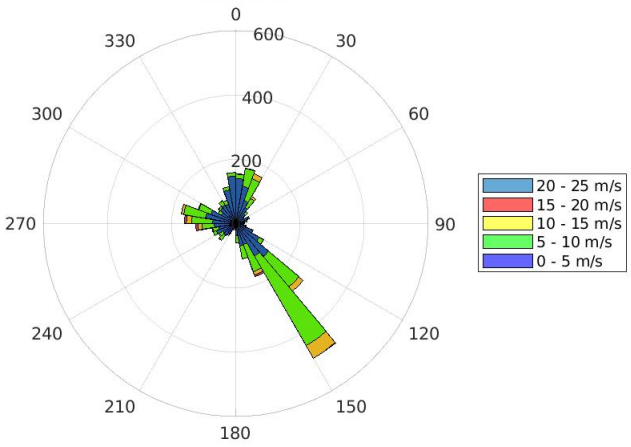

Figure 3.7: Example of a wind rose visualizing the wind direction, speed and number of occurrences from each direction where 0 indicates the north direction.

3.4 Turbine selection and power corrections

Three different wind turbines have been preselected from the criteria that the turbine should have a rated power below 1 MW. This criteria is chosen due to a less strict

concession process of turbines with rated power, or sum of rated power, less than 1 MW. The three chosen turbines are Enercon E-44, E-48, and E-54. Details of the turbines are listed in Table 3.2. From this table, one can observe that the cut-in and cut-out wind speed are the same for all turbines. The rated power is greater for E-44 compared to the other two.

Windturbine	Rated power [kW]	Cut-in [m/s]	Rated [m/s]	Cut-out [m/s]	Rotor diameter [m]	Hub height [m]
Enercon E-44	900	3	16.5	34	44	45
Enercon E-48	800	3	12	34	48	50
Enercon E-53	800	3	12	34	53	50

Table 3.2: Table of turbines below 1 MW and turbine specifications.

The power curve of each turbine is plotted in Figure 3.8. The output power from each of the turbine at different wind speeds are obtained from the manufacturer. The power curves from Enercon are calculated, and the calculations are based on; horizontal turbulence intensity of 12% and a standard air density $\rho_0 = 1.225$ kg/m^3 . From the figure, one can see that wind-speeds above 34 m/s do produce any power. Extreme wind events, i.e. above 34 m/s, is only interesting from the load and fatigue perspective. The figure shows that the rated power of the E-44 turbine is more significant than for the E-48 and E-54 turbines. Furthermore, the power output from the E-53 turbine is greater for weaker winds which is evident from the earlier rise of the graph.

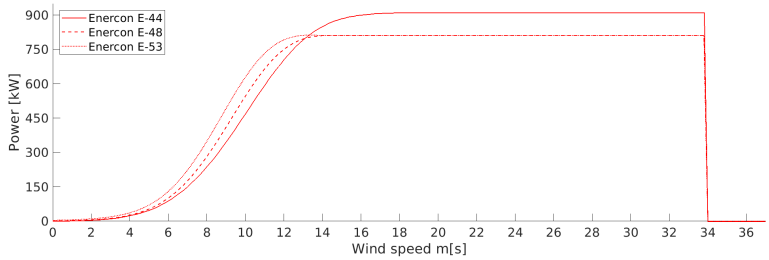

Figure 3.8: Power curve of the Enercon E-44, Enercon E-48, and Enercon E-53 turbine.

Turbulence corrections

Turbulence affects the power output from the turbine. A reduction is especially seen near the rated wind speed; thus it has to be considered. The categorization of TKE is very site-specific which is evident from [30] and [31] where a low TKE was below 0.4 m^{2}s^{-2}, and below 3.0 m^{2}s^{-2}, respectively. However, this thesis's TKE categorization is the same as used in [30] due to the most similarities in the surrounding terrain. Therefore, the amount of turbulence is divided into five categories according to the TKE values as appears from Table 3.3.

Turbulence category	TKE [m^2s^{-2}]
No	< 0.4
Very light	0.4 - 0.7
light	0.7 - 1.0
Moderate	1.0 - 1.4
Severe	> 1.4

Table 3.3: Turbulence categories and it's corresponding TKE value.

The amount of turbulence depends on several factors, and the characteristics of the topography in the area is one of them. Authors in [30] found that production losses approached 18% for winds above 9 m/s corresponding with high a TKE. A reduction was also seen for winds close to rated power in [31]. Furthermore, Authors in [31] found that a high TKE increased power production for weak winds. This is because there is more energy in rough winds, i.e. winds with a high degree of turbulence, as the wind's power varies as the cube of the with the wind speed[51]. However, only reductions due to turbulence are considered here. Corrections applied for severe turbulent conditions in this thesis are a power output reduction of 18 % for wind speeds above 9 m/s corresponding to a TKE above the severe threshold.

The wind farm at Vannøya, Fakken, have experienced production losses due to turbulent conditions from westerly winds due to formation of mountain waves[52]. There are similarities in the surrounding topography in the west at Fakken wind farm on Vannøya and in the fjords at Senja. Due to the strong reduction in power output at Fakken during westerly winds, it is reasonable to believe that the same is valid for Senja for very turbulent conditions. No power output is, therefore, assumed for winds corresponding to TKE above 3 m^2s^{-2}.

Chapter 4

Results and discussion

4.1 Data availability

Model data and observations from the observation sites stretch different periods as can be seen in Figure 4.2. Statistical scores and parameters have been calculated for the overlapping time periods in order to measure differences in model performance. The following section presents the quality of the models at the different locations.

In order to obtain a good comparison between model data and observations, the location of the observation site is essential. This is especially important in complex terrain; due to a higher wind shear and turbulence close to mountains, ridges, and steep slopes resulting in noise in the observations. Senjahopen and Innhesten are located close to Bringtinden and next to steep slopes, respectively. Comparison between forecasted values and observations from these locations are, therefore, expected to include some noise. The observation site at Hekkingen have, on the other hand, a considerable distance to the complex terrain. Less noise, i.e. turbulence, is expected at this location. Flow which are characteristic for complex terrain such as as gap winds and downslope windstorms would still affect the observations.

Model data are extracted from 10 magl at the grid point closest to the location of the observation site. The elevation of the model grid point, and the distance from closest grid point to the observation site, are dependent on the terrain data used in the model as well as the resolution of the model. The model topography, the location of closest grid point, and it's elevation can be seen if Figure 4.1. From the figure, one can observe that Arome 500 resolve the complex terrain better, i.e. fjords and steep slopes. At Innhesten, this is especially evident with a difference between real height of the terrain and model terrain of several hundred meters.

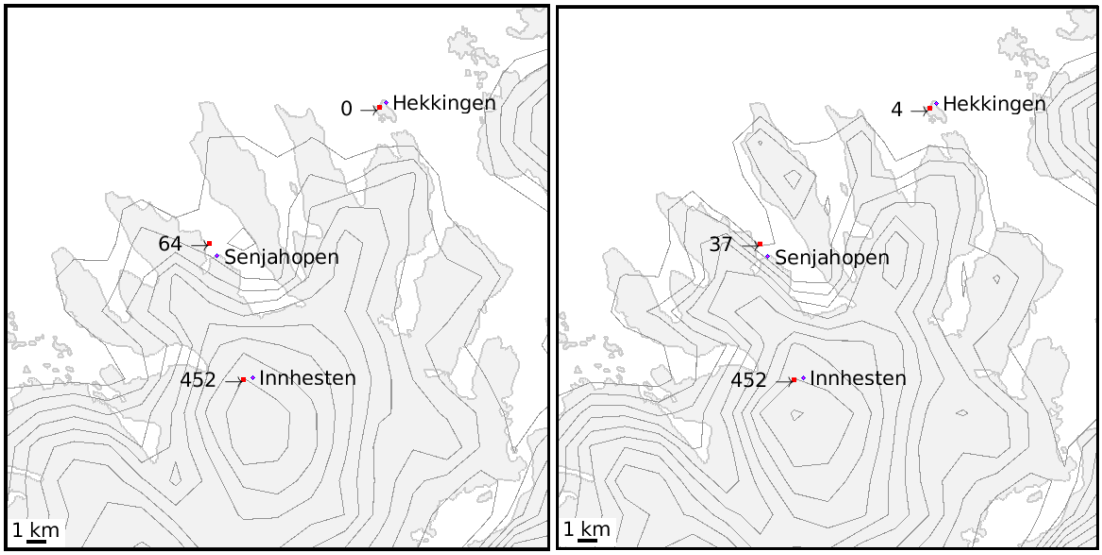

(a) NORA3 (b) AROME-Arctic

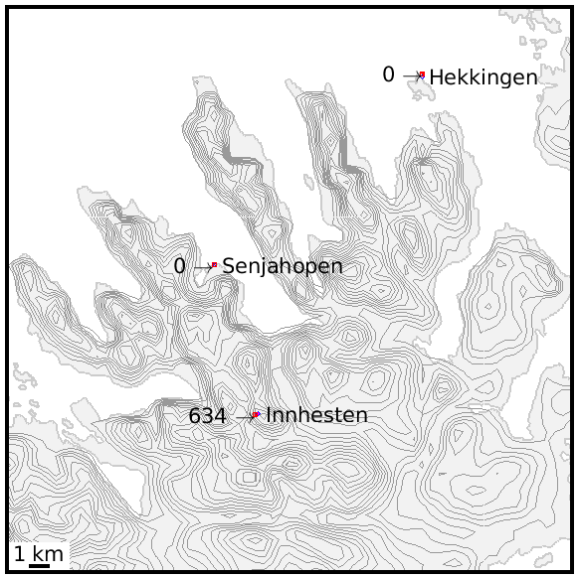

(c) Arome 500

Figure 4.1: The model topography. Red dots represent the location of the closest grid points used in the comparison between model data and observations. Furthermore, the numbers are height of the grid point in masl. The observation sites are marked with black dots.

All models are not overlapping the same time period as earlier mentioned. In order to compare the models over a year, NORA3 and AROME-Arcitc, and AROME-Arctic and Arome 500 are compared for different time periods. The green areas in Figure 4.2 show the overlapping period between Arome 500 and AROME-Arctic. The overlapping period between NORA3 and AROME-Arctic is in red. Statistical scores and parameters for wind speeds are calculated for the whole overlapping periods. Wind directions are compared by studying wind roses. Furthermore, the models are compared against each other by studying a map of the annual mean wind speed in

the overlapping periods as well as a strong wind situation 15 September 2019 at Hekkingen.

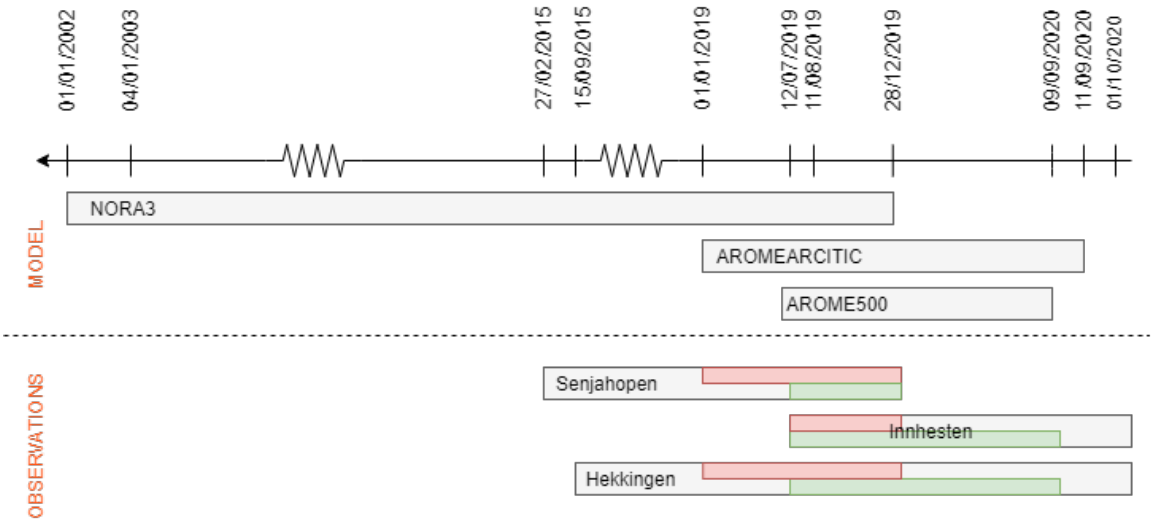

Figure 4.2: Timeline of the available datasets for models and observations. The comparisons witch is done for the overlapping periods are green for Arome 500 and AROME-Arctic and red for NORA3 and AROME-Arctic.

4.2 Model and observation comparison

4.2.1 Hekkingen

Observations from Hekkingen cover the period from 15 September 2015 to 1 October 2020. The yearly mean wind speed from 15 September 2015 to 15 September 2020 was 6.7 m/s. The overlapping period between NORA3 and AROME-Arctic cover the period from 1 January 2019 to 28 December 2019. Arome 500 and AROME-Arctic are compared in the period from 12 July 2019 to 9 September 2020. The two periods are characterized as low-wind periods for the location and have an average wind speed of 6.1 m/s and 6.0 m/s, respectively.

Prevailing wind directions

Figure 4.3 shows that the prevailing wind directions are from south-east at Hekkingen. The Malangen fjord in the south-east form gap winds, resulting in a high representation from this direction. Furthermore, winds from south-south-east also have a high representation at Hekkingen. Astritinden which ranges 742 masl stretches from Astrineset in north-west to Botnhamn in south. The mountain is steep in the west and east direction causing a deflection of winds from south and south-east. Winds

from the south, as well as winds deflected to the north by Astritinden, will accelerate down the lee slope towards Giska (see Figure 4.3) and further, to Hekkingen resulting in many winds from the south-south-east. Many observations of strong winds are also represented from the north and west.

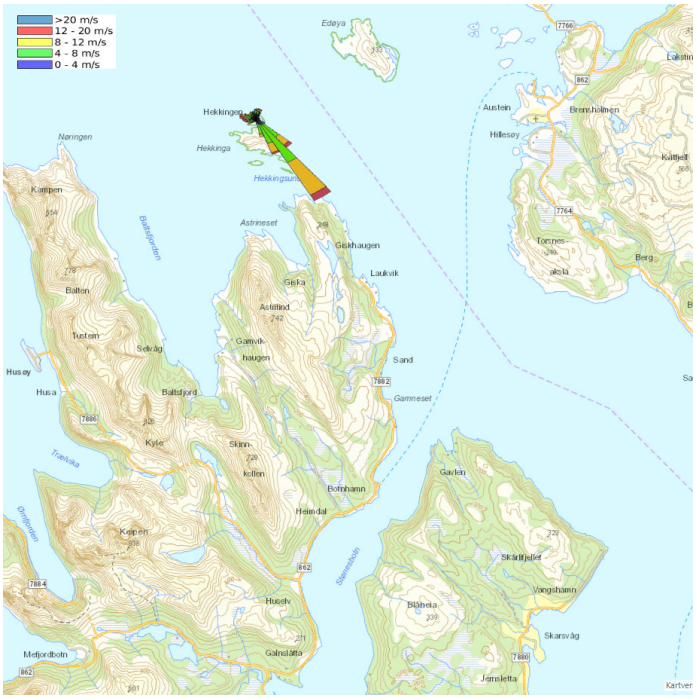

Figure 4.3: Map of the area around the observation site at Hekkingen with North direction facing up. Wind rose showing the relative distribution of winds at the location from 14 September 2015 to 14 September 2020. Colours are indicating speed intervals (NVE.no).

AROME-Arctic and NORA3

Winds	Model	RMSE [m/s]	ρ	MAE [m/s]	MBE [m/s]
All winds	NORA3	3,2	0,62	2,5	0,2
10 magl	AROME-Arctic	3,1	0,65	2,4	0,1
Weak winds (<12 m/s)	NORA3	3,0	0,41	2,4	-0,3
10 magl	AROME-Arctic	2,9	0,42	2,3	-0,3
Strong winds (>12 m/s)	NORA3	3,9	0,57	3,3	-2,9
10 magl	AROME-Arctic	4,2	0,51	3,5	-3,0
Strong winds (>12 m/s)	NORA3	8,1	0,00	6,9	-6,3
50 mgal	AROME-Arctic	3,8	0,52	3,0	0,4
Winter period	NORA3	3,5	0,63	2,8	-0,2
10 magl	AROME-Arctic	3,4	0,64	2,7	-0,2
Summer period	NORA3	3,0	0,51	2,3	0,6
50 magl	AROME-Arctic	2,8	0,57	2,1	0,5

Table 4.1: Calculated verification scores in the overlapping period between AROME-Arctic and NORA3.

The overlapping period for AROME-Arctic and NORA3 are from 1 January 2019 to 28 December 2019. 99.8% was avaliable for analysis in this time period. From the MBE for all winds in Table 4.1, one can observe that the models slightly over-predicted the period's wind speed. AROME-Arctic had a MBE of 0.1 m/s, and NORA3 had a MBE of 0.2 m/s. AROME-Arctic had smaller errors than NORA3 for all winds, as evident from the MAE and RMSE in the table. The correlation was 0.65 for AROME-Arctic and 0.62 for NORA3, indicating small differences between the models.

From the table, one can observe that the models underpredicted the weak winds. The MBE was -0.3 m/s for both models. Furthermore, the MAE and RMSE were a bit higher for NORA3 for the weak wind, as shown in the table. The correlation was slightly better for AROME-Arctic for these winds. The higher correlation coefficient for strong winds compared to weak winds are as expected. Weak winds in the observations could arise from subscale processes that vary largely in space and time. However, both models underestimated the strong winds with a MBE of -3.0 m/s for AROME-Arctic, and -2.9 m/s for NORA3.

AROME-Arctic had larger errors for stronger winds than NORA3, which appear from the RMSE score in Table 4.1. From the 50 magl wind speed calculations, one can observe that the MBE for AROME-Arctic is positive 0.4 m/s. This may indicate that a large negative MBE for strong winds 10 magl results from a large vertical distance between the grid point height and the height of the observation site. The wind 50 magl is for AROME-Arctic linearly interpolated between wind speed 20 and 80 magl. The vertical wind profile between these heights are not necessarily linear and the interpolation may deviate from actual 50 magl model values if they were extracted. One can also observe that the wind speed 50 magl extracted from NORA3 has large errors in speed, and most likely in time due to no correlation between the model data and observations.

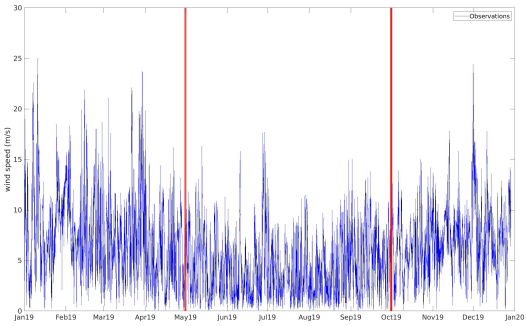

Figure 4.4: Time series of the observations at Hekkingen in the overlapping period between NORA3 and AROME-Arctic.

Wind roses for Hekkingen is shown in Appendix A: *Wind roses Hekkingen*. The predicted wind directions are similar for both NORA3 and AromeArctic. This is valid for both weak and strong winds. The prevailing wind directions at the observation site in the overlapping period are from north to north-west, and south to south-east. Both

models capture this pattern. However, there is a too high density of winds from north to west and south-west for the weak winds in both models. The overrepresentation of weak winds from these directions are especially evident in NORA3. For stronger winds, both models show the same directional pattern as the observations.

The winter period is defined in this thesis as the period from October to the end of April. The summer period is defined as the period from May to October. The winter period is a period characterized by higher mean wind speed as is evident from Figure 4.4. The overlapping winter period for NORA3 and AROME-Arctic are from 1 January 2019 to 31 April 2019 and 1 October 2019 to 28 December 2019. The mean wind speed for the period is 7.5 m/s. The MBE and correlation for both models are -0.2 and 0.6 m/s, respectively. The RMSE is 3.4 m/s for AROME-Arctic and 3.5 m/s for NORA3. Both models showed, in other words, more or less the same verification scores in the winter period. From the wind roses in the appendix, one can observe that the model predicted too few winds from the south-east and too many winds from south-west compared to the observations.

The summer period is characterized with weaker winds, as shown in Figure 4.4. The mean wind speed drops to 4.7 m/s in this period. The correlation coefficient is 0.57 for AROME-Arctic and 0.51 for NORA3, as shown in Table 4.1. Both models slightly overestimated for the period. The MAE is 2.1 m/s and 2.3 m/s for AROME-Arctic and NORA3, respectively. From the wind roses, one can observe that both models show few winds from south to south-east, and many winds from north-east compared to the observations.

Arome 500 and AROME-Arctic

Winds	Model	RMSE [m/s]	ρ	MAE [m/s]	MBE [m/s]
All winds	Arome 500	2,9	0,71	2,3	0,3
10 magl	AROME-Arctic	3,1	0,68	2,4	0,4
Weak winds (<12 m/s)	Arome 500	2,8	0,51	2,2	-0,1
10 magl	AROME-Arctic	2,9	0,45	2,3	-0,1
Strong winds (>12 m/s)	Arome 500	3,8	0,49	2,9	-2,3
10 magl	AROME-Arctic	3,7	0,54	2,9	-2,2
Strong winds (>12 m/s)	Arome 500	3,4	0,51	2,6	-0,8
50 mgal	AROME-Arctic	3,6	0,56	2,8	0,9
Winter period	Arome 500	3,2	0,66	2,4	0,6
10 magl	AROME-Arctic	3,3	0,64	2,6	0,3
Summer period	Arome 500	2,7	0,63	2,2	0,3
50 magl	AROME-Arctic	2,9	0,62	2,3	0,7

Table 4.2: Calculated verification scores in the overlapping period between Arome 500 and AROME-Arctic.

The overlapping period between Arome 500 and AROME-Arctic is from 12 July 2019 to 9 September 2020. Both models overestimated the wind speed for this period, as

shown in Table 4.2. Arome 500 had a higher correlation coefficient of 0.71 for this period compared to AROME-Arctic. The RMSE show that Arome 500 had smaller errors compared to AROME-Arctic. The table shows that both models had a very low MBE of 0.1 m/s. The correlation coefficient were 0.51 and 0.45 for Arome 500 and AROME-Arctic, respectively.

AROME-Arctic shows a high degree of directional correlation for the weak winds, evident from the wind roses in Appendix A *Wind roses Hekkingen*. Arome500 predicts too many winds from east, north-east, south, and south-west. However, the model captures the main pattern with winds from south to south-east. For stronger winds, both models underestimated the wind speed. A slightly higher RMSE value indicates that Arome 500 have more large errors compared to AromeArctic. The correlation coefficient for stronger winds are 0.49 for Arome 500 and 0.54 for AROME-Arctic. The correlation was greater, and the MBE was closer to 0 m/s for both models for winds 50 magl.

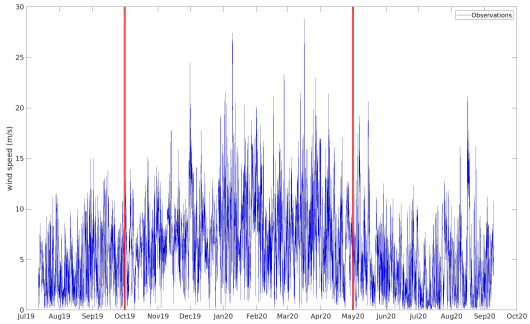

Figure 4.5: Time series of the observations at Hekkingen in the overlapping period between Arome 500 and AROME-Arctic.

A clear seasonal pattern appears for this period and can be seen in Figure 4.5. The winter period have a mean wind speed of 8 m/s. Table 4.2 shows that both models overpredicted the wind speed for this period. The correlation coefficient for the winter period is 0.66 for Arome 500 and 0.64 for AROME-Arctic. The RMSE value was slightly higher for AROME-Arctic as can be seen in the table. From the wind roses in Appendix A *Wind roses Hekkingen*, one can observe that AROME-Arctic predict too many winds from the south. Arome 500 show the same directional pattern as in the observations. In the summer period, the mean wind speed drops to 4.3 m/s. The correlation coefficient is 0.63 and 0.62 for Arome 500 and AROME-Arctic, respectively. Furthermore, AROME-Arctic has a larger MBE and RMSE compared to Arome 500 for this period.

Temperature comparison

Model	ρ	MAE [°C]	MBE [°C]
NORA3	0,98	1,0	0,0
AROME-Arcitc	0,97	1,0	0,0
Arome 500	0,97	1,2	-0,6
AROME-Arctic	0,98	1,0	0,0

Table 4.3: Calculated verification scores for temperature in both overlapping periods

Temperatures are also available from the Hekkingen dataset, and calculated verification scores can be seen in Table 4.3. The model temperature correlates well with the observed temperatures. The lowest correlation coefficient is 0.97 in the overlapping periods for all models. AROME-Arctic and NORA3 had 0°C MBE for the whole overlapping period. The MAE was only 1°C for both. Arome 500 under predicted the temperatures in the overlapping period between Arome 500 and AROME-Arctic. Arome 500 has a MBE -0.6°C and a MAE of 1.2°C. Arome 500 and AROME-Arctic have a lower correlation coefficient from December to May compared to the period from May to December. Generally, all models slightly underpredict the summer-period temperatures from May to October and over predicted in the winter from October to May.

4.2.2 Senjahopen

Observations from the Senjahopen observation site stretches from 27 February 2015 to 28 December 2019 as can be seen in Figure 4.2. In 2019, no observations was obtained until 27 February 2019. The overlapping period between NORA3 and AROME-Arctic is, therefore, not a full year. The overlapping period between Arome 500 and AROME-Arcitc is only six months for Senjahopen. Furthermore, only 8 observations was above the strong wind threshold for this period thus statistical scores and parameters are only calculated for all winds. The mean wind speed in the observations was 2.6 m/s and 2.4 m/s for NORA3 and AROME-Arctic, and Arome 500 and AROME-Arctic, repsectively.

Winds	Model	RMSE [m/s]	ρ	MAE [m/s]	MBE [m/s]
All winds	NORA3	2,5	0,66	1,8	1,5
10 magl	AROME-Arctic	2,5	0,60	1,9	1,3

Table 4.4: Calculated verification scores in the overlapping period between NORA3 and AROME-Arctic at Senjahopen.

From Table 4.4 one can observe that both models predict too strong winds on average for this period. NORA3 have a slightly higher correlation coefficient for the

whole period compared to AROME-Arctic. Wind roses for the overlapping periods at Senjahopen can be seen in Appendix B: *Wind roses Senjahopen*. From these one can observe that very few winds are represented from the north and from the south-east in the observations compared to the models. This might be a result of the location of the observation site on the north west side of Bringtinden. The mountain seem to block winds from the south-east as well as reduce the wind speed for winds from the north-west. Furthermore, from Figure 4.1 the model grid point is located almost 1 km north-west of the observation site. The figure also show that Bringtinden and the rest of the surrounding topography are poorly resolved, and the effect on the wind flow due to the complex topography can, therefore, not be expected resolved.

Winds	Model	RMSE [m/s]	ρ	MAE [m/s]	MBE [m/s]
All winds	Arome 500	2,6	0,48	1,9	1,0
10 magl	AROME-Arctic	2,5	0,62	1,9	1,4

Table 4.5: Calculated verification scores in the overlapping period between Arome 500 and AROME-Arctic at Senjahopen.

12 July 2019 to 31 December 2019 are the overlapping period between Arome 500 and AROME-Arctic at Senjahopen. From Table 4.5 one can observe that both models overestimates on average the wind speed for the period, but AROME-Arctic slightly more. From Fiugre 4.1c one can observe that Arome 500 manage to resolve Bringtinden and the surrounding complex terrain better. From the wind roses in Appendix B: *Wind roses Senjahopen*, one can observe that the retardation of wind from north-west in front of Bringtinden are resolved by Arome 500. However, there is a too high representation of winds from the south-east, and especially to strong winds. AROME-Arcitc predict to many winds from both the north-west and south-east.

The highly complex terrain and Bringtinden just south of the observation site disturb the wind patterns. As discussed for weak winds in Section 4.2.1, the weak winds could arise from sub-scale processes which varies largely both in space and time. Since the mean wind speed is so low at the location, the correlation between observations and model results are not expected to be high. Furthermore, the Arome 500 model captures the flow patterns best at the location based on visual comparison of the wind roses. Due to short timespan of the overlapping periods, as well as the locations low mean wind speed, few conclusions regarding the relation between Arome 500 and NORA3 can be made from this location.

4.2.3 Innhesten

Observations from Innhesten stretches the time period from 11 August 2019 to 1 October 2020. The overlapping period between NORA3 and AROME-Arctic cover, therefore, only the last 5 months of 2019. The overlapping period between Arome 500 and AROME-Arctic cover a full year from 11 August 2019 to 11 August 2020.

The height of the grid point, as well as the distance to the observation site, can be seen in Figure 4.1. As earlier mentioned, the observation site is located on top of the mountain Innhesten 915 masl; thus, the height of the model grid points deviates with several hundred meters from the actual height of the mountain.

Winds	Model	RMSE [m/s]	ρ	MAE [m/s]	MBE [m/s]
All winds	NORA3	2,8	0,60	2,2	-0,6
10 magl	AROME-Arctic	2,9	0,57	2,2	-0,6
Weak winds (<12 m/s)	NORA3	2,7	0,46	2,2	-0,8
10 magl	AROME-Arctic	2,8	0,42	2,2	-0,8
Strong winds (>12 m/s)	NORA3	5,8	0,12	5,3	-4,5
10 magl	AROME-Arctic	5,7	0,18	5,3	-4,6

Table 4.6: Calculated verification scores in the overlapping period between AROME-Arctic and NORA3 at Innhesten.

From Table 4.6 one can observe that both NORA3 and Arome Arctic show almost similar scores for all winds, weak winds, and for strong winds. Furthermore, from the table, both models have a low negative MBE and a large MAE for all winds and weak winds. For strong winds, the MBE and MAE are both large. From the wind roses in Appendix C: *Wind roses Innhesten* , one can see that both models' directional distribution deviate from the observed wind directions.

The table shows that Arome 500 and AROME-Arcitc have approximately the same verification scores for all winds and weak winds. For strong winds, AROME-Arctic had a significant higher correlation coefficient compared to Arome 500. Wind roses for the overlapping periods at Innhesten are shown in the appendix. These show that the models do not predict the same patterns as the observed. This is especially evident for Arome 500, which predicts very few winds from the south-east and north.

Winds	Model	RMSE [m/s]	ρ	MAE [m/s]	MBE [m/s]
All winds	Arome 500	3,5	0,63	2,6	-0,7
10 magl	AROME-Arctic	2,9	0,67	2,2	-0,4
Weak winds (<12 m/s)	Arome 500	3,4	0,50	2,7	-0,6
10 magl	AROME-Arctic	2,8	0,50	2,2	-0,4
Strong winds (>12 m/s)	Arome 500	5,7	0,24	4,8	-3,4
10 magl	AROME-Arctic	4,9	0,44	4,3	-3,6

Table 4.7: Calculated verification scores in the overlapping period between Arome 500 and AROME-Arctic at Innhesten.

Large negative errors for all models in both overlapping periods, especially for strong winds, probably due to the large difference between the height of the mountain and the height of the model topography. The steep slopes and complex topography surrounding the observation site are expected to generate turbulence. This especially evident for the strong winds, where the RMSE, MAE, and MBE are high, and the

correlation is low. Furthermore, only 5 months of overlapping data between AROME-Arctic and NORA3 was possibly the cause of a low correlation coefficient for weak and for strong winds.

4.3 Model comparison

Figure 4.6a and 4.6b show the mean wind speed in the overlapping between NORA3 and AROME-Arctic in the period from 1 January to 28 December 2019. From the figures, one can observe that the model shows the same patterns; the annual mean wind speed increases from the south-east towards the north-west. The fjords, the slopes, and the narrow mountain ridges surrounding Senjahopen and Husøy show no variations in yearly mean wind speed as expected due to the complex topography in combination with a horizontal resolution of the model wider than the fjords at the location. Furthermore, the Malangen fjord south-east of Hekkingen are characterized with higher mean wind speed in both models. Figure 4.1a and 4.1b, it is evident that the narrow fjords and steep mountains around Senjahopen and Husøya are unresolved whereas the wider strait south-east of Hekkingen is resolved. Due to this, the model resolves the gap winds formed in the Malangen fjord from the south-east as discussed in Section 4.2.1, but not in the narrow fjords around Senjahopen and Husøy.

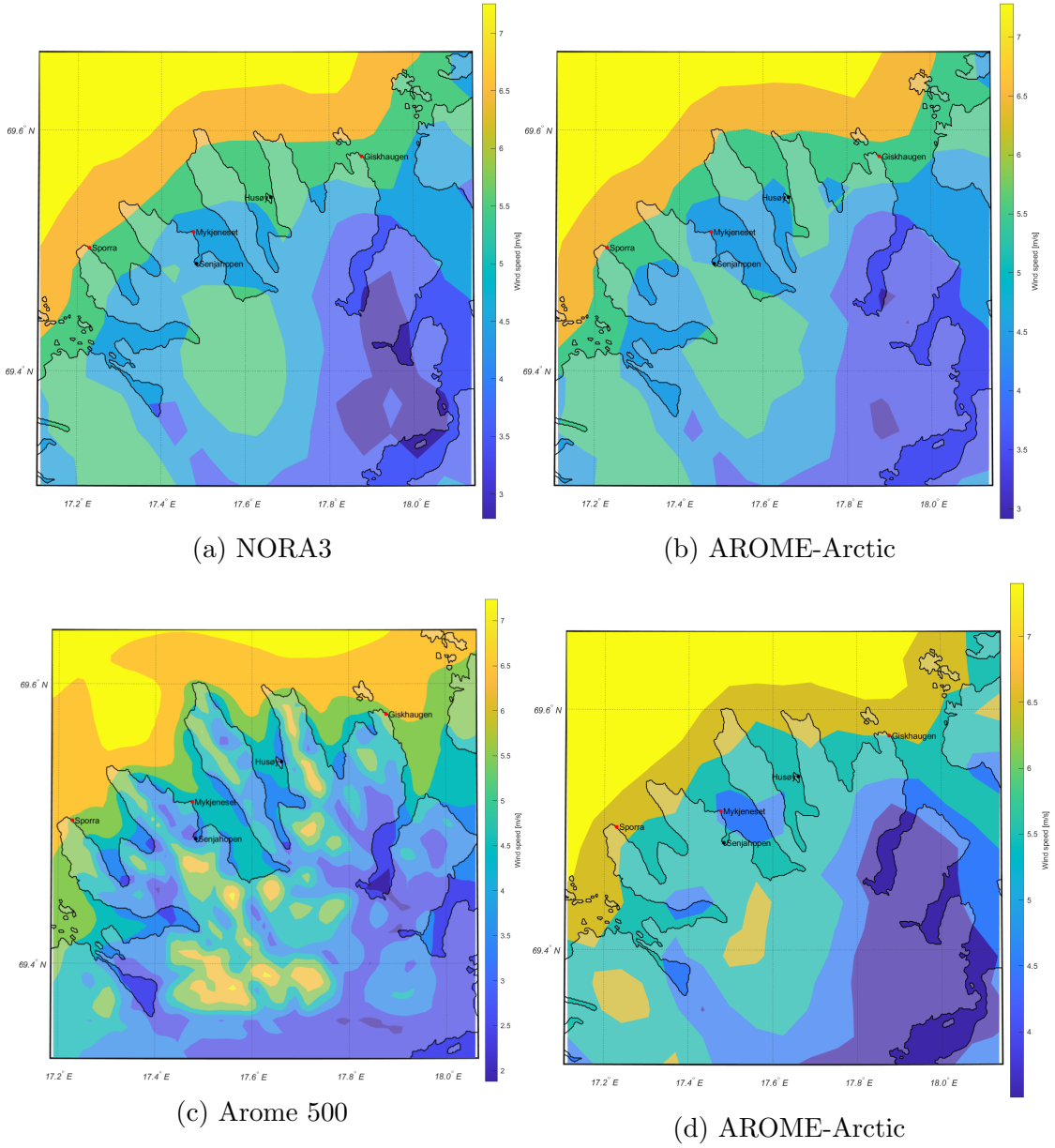

(a) NORA3

(b) AROME-Arctic

(c) Arome 500

(d) AROME-Arctic

Figure 4.6: Mean wind speed for the overlapping periods where (a) and (b) are the overlapping period between NORA3 and AROME-Arctic, and (c) and (d) are the overlapping period between Arome 500 and AROME-Arctic

Figure 4.6c and 4.6d show the mean speed over northern Senja in the overlapping period between Arome 500 and AROME-Arctic. First, AROME-Arctic show more or less the same patterns as for the overlapping period with NORA3. Arome 500, on the other hand, predicts a higher wind speed in the fjords and on the mountain ridges. From the topography map in Figure 4.1c, the fjords and complex terrain are resolved as earlier discussed. Due to this, the complex terrain flow such as gap winds in the narrow fjords, and downslope winds behind ridges seem to be resolved by the model.

Figure 4.7 show the predicted wind speed and direction 10 magl by the models on 15 September 2019 07:00 UTC. The observation showed strong winds with a

magnitude of 13.8 m/s from south-east at Hekkingen whereas the wind speed and direction at Senjahopen and Innhesten were 3.0 m/s from north 10.4 m/s from the east, respectively. From the figure on can see that Arome 500 in Figure 4.7c predicts stronger winds in the fjords than AROME-Arctic and NORA3. This is especially evident in the fjord where Senjahopen is located. Gap winds accelerate from the innermost part of the fjord and out of the fjord gap where the highest wind speeds are observed. Furthermore, higher winds are also present in the innermost part of the fjord due to winds accelerating down the lee towards the fjord. However, south-east of Hekkingen, NORA3 and AROME-Arctic predicts the strongest winds, but the fjord's canalisation is more evident in Arome 500.

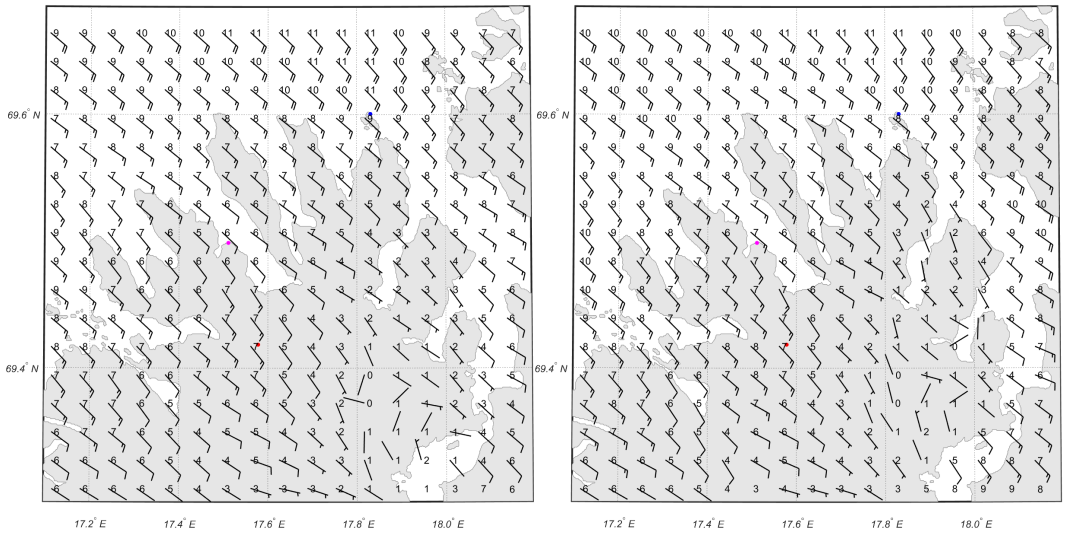

(a) NORA3 (b) AROME-Arctic

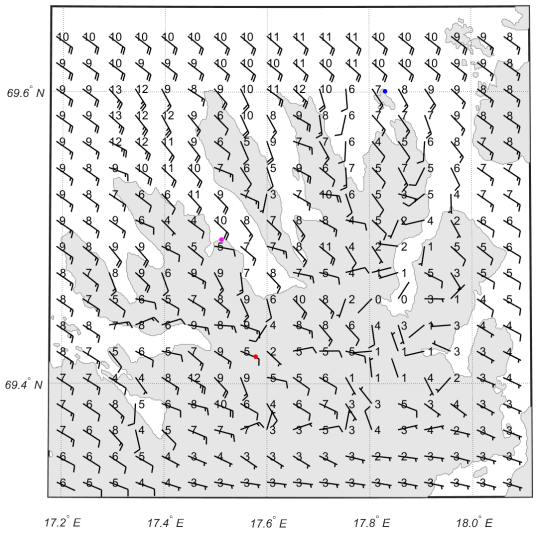

(c) Arome 500

Figure 4.7: Strong winds predicted by the models 15 September 2019 07:00 UTC 10 magl. The red, purple and blue dots are the location of Innhesten, Senjahopen, and Hekkingen, respectively

4.4 Summary comparison

At Hekkingen, Arome 500 and AROME-Arctic showed very small differences in error and correlation coefficient for all winds, the weak winds and for the summer period. The same was for AROME-Arctic and NORA3 in their overlapping period. For strong winds, all models had a large negative MBE which may result from the height difference between the anemometer 43 masl and the grid point predicted values 10 masl. Comparisons of winds from the models at 50 magl had higher correlations as well as lower MBE and MAE except for NORA3 which had large errors and smaller correlation possibly due to some time lag error in the data extraction from the model. Since windspeed 50 masl had to be linearly interpolated between 20 and 80 masl in AROME-Arctic, and NORA3 had very large errors, Arome 500 is considered best for the strong winds. A comparison between the NORA3 dataset and Arome 500 can not be made for strong winds 50 magl at this location. Temperatures was also available at Hekkingen. All models showed small errors and a high correlation coefficient, both in the summer period and in the winter period.

The observation site at Innhesten was located several hundred meters above the grid points. The model predicted wind speeds had almost no correlation against the observations as well as large errors. For weak winds and all winds the models scored almost the same in both overlapping periods. However AROME-Arctic had a significantly higher correlation for strong winds. Directionally, all models struggled to predict the correct directional distribution. However, among the models, NORA3 and AROME-Arctic showed the best results, and for locations similar to this, the NORA3 dataset seem to be the best choice in the wind resource assessment.

Observations from Senjahopen showed that Bringtinden slowed down the winds from north and created a wind shadow for winds from south and south-east. The Arome 500 captured the pattern of retardation of winds from north. AROME-Arctic and NORA3 did not manage to resolve the complex terrain thus did not capture this pattern. Furthermore, the mean wind speed was 2.4 m/s and 2.6 m/s in both overlapping periods. Such weak winds may stem from small scale processes in the atmosphere thus good model result are hard to obtain. From the verification scores Arome 500 showed the lowest MBE and NORA3 showed the highest correlation. However, from the wind roses and calculated statistical scores at Senjahopen it's hard to conclude which model showed the best results at this location. From Section 4.3, it was evident that gap winds and downslope windstorms was resolved with the Arome 500 model but not in NORA3 and AROME-Arcitc.

The overlapping period between Arome 500 and AROME-Arcitc was only 6 months at Senjahopen, and the overlapping period between NORA3 and AROME-Arctic was only 4 months at Innhesten. The MAE, MBE, and correlation did also vary significantly for the models at both Innhesten and Senjahopen. Therefore no clear statement of the correlation between NORA3 and Arome 500 can be set on the basis of these observation sites. At Hekkingen, it was found that NORA3 had large errors for winds 50 magl which probably was due to a an error when extracting the data due to almost 0 correlation. thus no scaling factor for the NORA3 dataset was found

from the verification which could increase its accuracy, thus provide a longer dataset in the power assessment. The Arome 500 model are, therefore, the only used model in further sections.

4.5 Wind resources

This section's scope is to present locations that might be suitable for wind power production at northern Senja. The area of interest is neighbouring areas close to Senjahopen and the small island Husøya. Maps of the yearly mean wind speed, TKE, and map of established road and grid lines are used.

Areas with high mean wind speed are most interesting as potential sites for wind power generation. Figure 4.8 shows a contour plot of the yearly mean wind speed from 9 September 2019 to 9 September 2020 predicted by Arome 500. The data are bi-linearly interpolated between the grid points by the contourm function in MatLab[1]. The map is projected by using Lambert conformal conic projection (LCC).

[1]Matlab is a programming platform used in this thesis to compute statistical scores, and parameters, as well as visualizing the data from observations, and model in the form of plots, and wind roses.

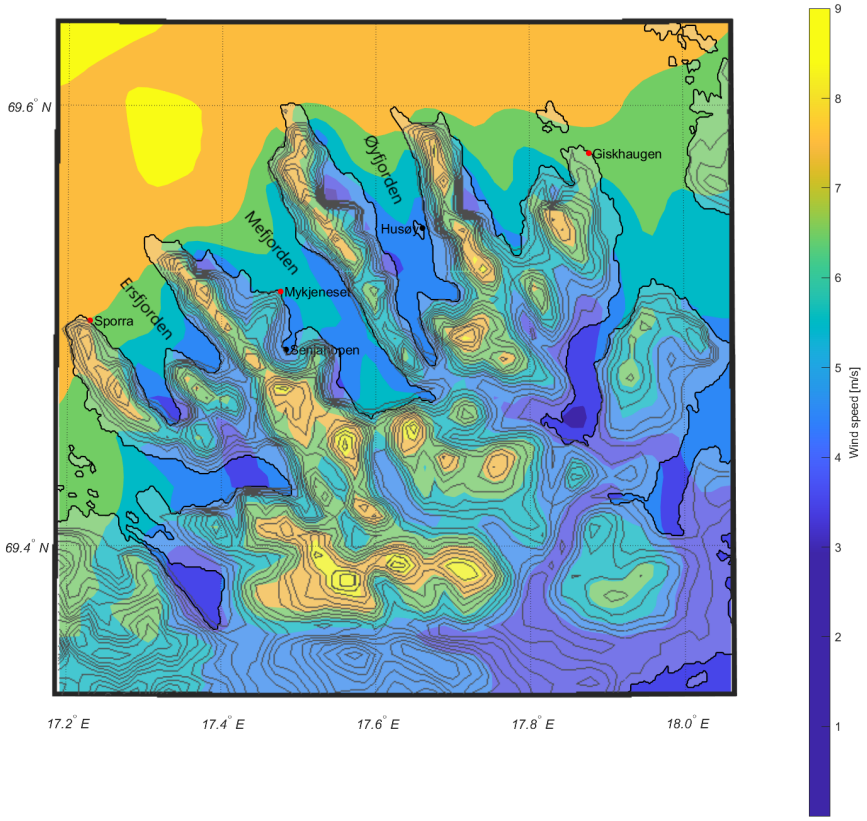

Figure 4.8: Contour plot of the yearly mean wind speed from Arome 500 η-layer 86 approximatly 48 magl in the period from 9 September 2019 to 9 September 2020 over northern Senja. Senjahopen and Husøy are marked with black dots. The solid black line is the shoreline, whereas the solid grey lines are the calculated height from the geopotential in Arome 500. The vertical distance between each grey line is 50 meters.

In addition to the yearly mean wind speed, the yearly mean of TKE is mapped, as shown in Figure 4.9. The predicted values of TKE are obtained from Arome 500 on η-layer number 86, which corresponds to 48 magl. The turbine location should be placed where there is a minimum of turbulence for the higher wind speeds. This is due to material fatigue and in order to obtain as high power output as possible from the wind turbine as described in Chapter 2, Section 2.3.

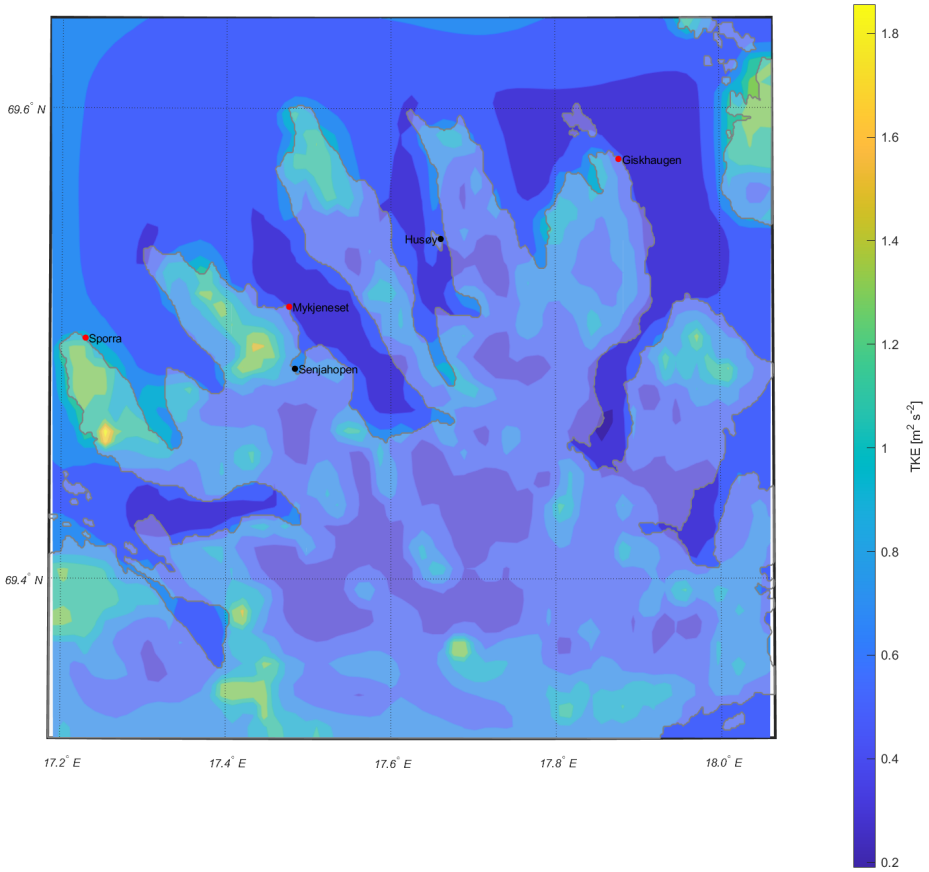

Figure 4.9: Contour plot of the yearly mean TKE in the period from 9 September 2019 to 9 September 2020 over northern Senja. The light grey line are the shoreline.

The topography, the established grid, and main roads in the neighbouring area around Husøy and Senjahopen are shown in detail in Figure 4.10. The existing power grid is shown as solid green and blue lines. The green lines represents a 22 kV power line, whereas the blue line represent a 132 kV power line. The red squares are transformer stations, and the main roads are solid yellow lines.

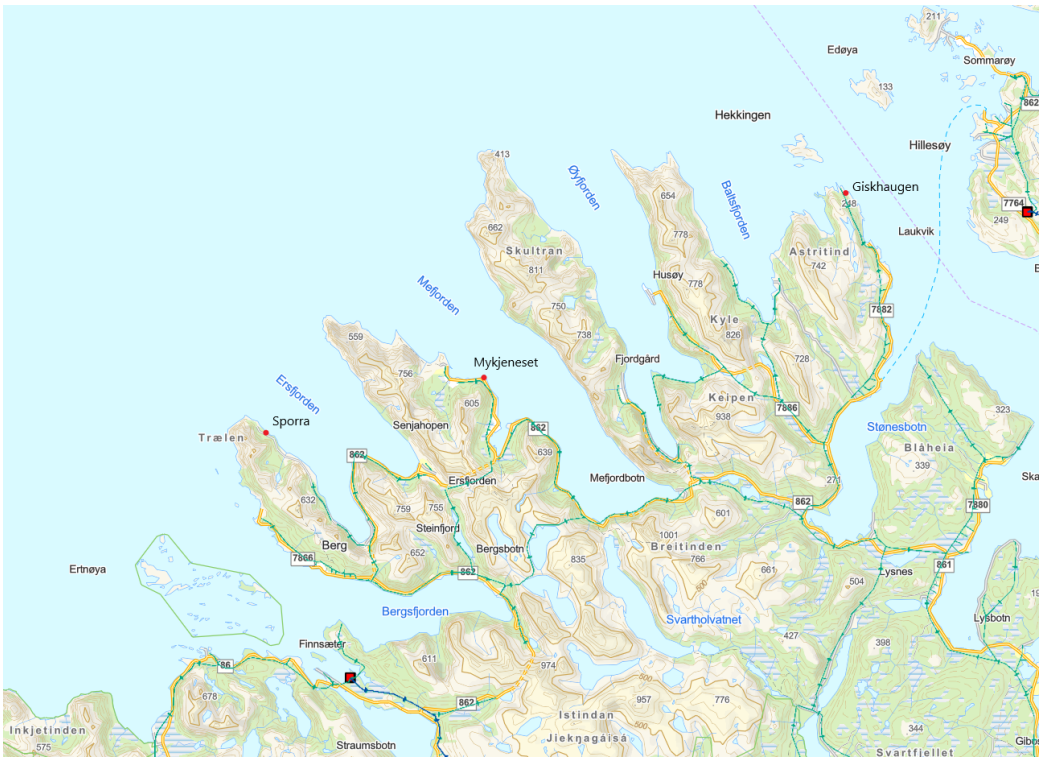

Figure 4.10: Topography map of northern Senja which show the existing $22kV$, and $132kV$ power lines as green, and blue lines, respectively. The red boxes are transformer stations, and yellow solid lines are main roads.

Figure 4.8 shows that a high yearly mean wind speed is characterized by mountain tops and ridges. These areas are not suitable locations due to economic aspects related to establishing power lines, roads and other infrastructure in the steep terrain.

Winds in the innermost part of the fjords on northern Senja are characterized by a lower mean wind speed of 4-5 m/s whereas the outermost parts of the fjords have a higher mean wind speed of 5-8 m/s as can be seen in Figure 4.8. The higher mean wind speed in the fjords' outermost parts might be due to gap winds accelerating when leaving the fjord. Furthermore, some of the fjords, e.g. Mefjorden also have an area of high mean wind speed in the innermost parts of the fjord. This might be due to downslope windstorms accelerating down the lee slope in the innermost part of the fjord. However, downslope windstorms are more turbulent compared to the gap winds. The outermost parts of Ersfjorden and Mefjorden and the area south of Hekkingen, are, therefore, examined closer. The area around Husøya, namely Øyfjorden, the south-east to north-west oriented fjord north of Mefjorden also has a high yearly mean wind speed. However, the fjord has very complex topography and no established grid lines or roads, on any side of the fjord as can be seen in Figure 4.10. Øyfjorden is, therefore, not examined closer.

Steep mountain slopes straight to the ocean characterize the north-east side of Ersfjorden, and no infrastructure is established here, as shown in Figure 4.10. The mean wind speed on the west side of the fjord has its highest value at Sporra

and decreases gradually to the fjord's innermost part as shown in Figure 4.8. The turbulence is more severe in the outermost parts of the fjord as expected due to high mean wind speed and the proximity to the steep, complex terrain. However, just south of Sporra, the TKE value indicates only light turbulence and a high yearly mean wind speed. On the SW side of the fjord, A 22 kV power line is established, which are shown in Figure 4.10. Furthermore, a road are already established all the way to the red dot marked as Sporra in the figure (not visible in Figure 4.10.

A high yearly mean wind speed is predicted by the model on the south-west side of Mefjorden past Mykjeneset. Very light to no turbulence is predicted along the south-west side of the fjord. Power lines and roads are already established, as can be seen in Figure 4.10. The north-east side of Mefjorden compared to the south-west side are characterized by steep mountain slopes straight to the ocean, no existing roads nor power lines, higher TKE, and lower yearly mean wind speed. Only the south-west side of the fjord are, therefore, interesting from the viewpoint of wind-energy production.

Giskhaugen, just south of Hekkingen, has a high yearly mean wind speed, as shown in Figure 4.8. The Malangen fjord in the south-east direction canalizes the wind towards Giskhaugen and Hekkingen as discussed in section 4.2.1. The topography is less complex compared to the fjords in the west. The TKE map in Figure 4.9 indicates that there is on average no to light turbulence in this area. Power lines already exist to Giskhaugen, and the main road is established to Laukvik, as can be seen in Figure 4.10.

The locations of Sporra in Ersfjorden, Mykjeneset in Mefjorden, and Giskhaugen south-east of Hekkingen are examined closer in the next sections.

4.5.1 Prevailing wind directions

A scatter plot of the wind speed, and its corresponding direction for each location in the time period from 9 September 2019 to 9 September 2020 is plotted in Figure 4.11.

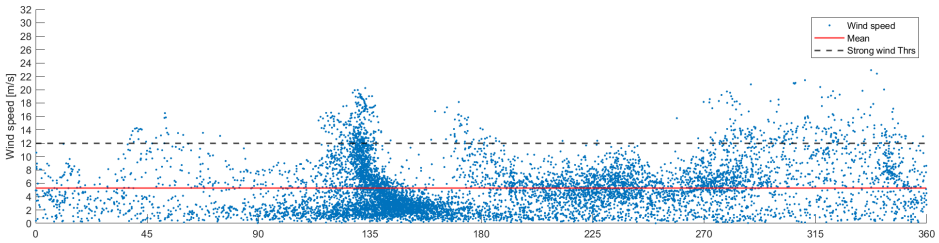

(a)

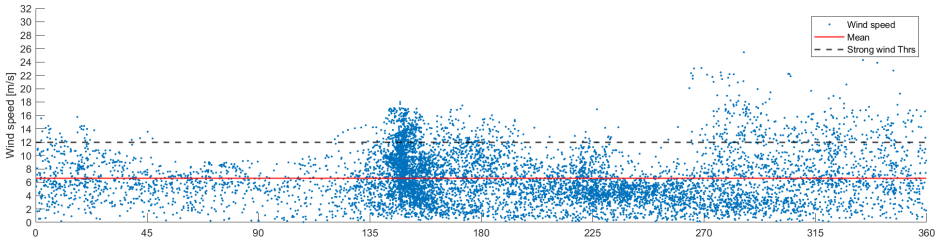

(b)

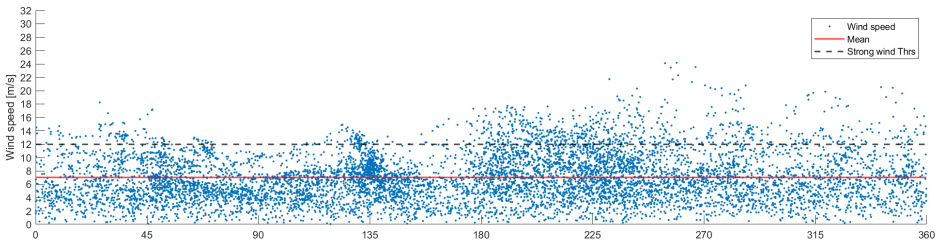

(c)

Figure 4.11: Scatter plot of the wind speed and direction at (a) Mykjeneset, (b) Giskhaugen, and (c) Sporra. The solid red line represents the mean wind speed at the location, and the dashed green line represents the strong wind threshold. The wind direction in degrees represents the direction where the wind is blowing from. That means that wind from 135° are wind from south-east.

Mykjeneset is located just north of Senjahopen along the south-east north-west oriented Mefjorden. Figure 4.11a shows that the prevailing wind direction is from south-east. The highest frequency of strong winds, i.e. above 12 m/s, are also from south-east. Some high wind events are also from the north-west. This is a result of the canalization of winds in the south-east north-west oriented fjord. Strong wind events from the west are probably due to downslope winds formed by mountains in the west (see Figure 4.10). Few strong-wind events are from south-west, and north to north-east. From Figure 4.8 and 4.10, one can observe that high mountains is present there creating a wind shadow for winds from these directions.

Giskhaugen is located in the south-east direction of Hekkingen, as shown in Figure 4.10. From Figure 4.11b one can observe that the prevailing wind direction at the location is from south to south-east. The main cause of this is most likely due to gap-winds formed in the Malangen Fjord, south-east of the location, as discussed in Section 4.2.1. Furthermore, strong winds are also represented from the north.

Sporra is located in the outermost part of Ersfjorden as shown in Figure 4.10. From the scatter plot in Figure 4.11c one can observe a marginal higher density of winds from the SE compared to the other directions. However, almost all winds from this direction is below the strong wind threshold. The prevailing wind directions for strong winds are from south-west. This is possibly due to downslope windstorms from the mountains south-west and west of the location (see Figure 4.10).

4.5.2 Turbulence

The topography on northern Senja is as earlier described mountainous and complex. More turbulence is expected in complex terrain compared to open areas, for strong and weak winds. The amount of turbulence is thus taken into account to obtain better evaluations of the locations and more accurate production estimates. The amount of turbulence are divided into five categories according to the TKE value. The five turbulence categories and its corresponding TKE values are all listed in Table 3.3.

Figure 4.12a represents the TKE at Mykjeneset. The figure shows that the predicted turbulence at the location falls under the category light turbulence from Table 3.3. Most observations below the light threshold are also wind speeds below the threshold for strong winds, i.e. 12 m/s. However, many observations above the strong wind threshold are below a TKE of 1 m^2s^{-2} from the south-east, which is also the prevailing wind direction at the location. For winds from south-west to west, many weak winds generate high TKE. This might be due to the proximity of the location to steep mountains from this direction which generates downslope windstorms.

Figure 4.12b represents the TKE at Giskhaugen. The mean TKE is lower at Giskhaugen than Mykjeneset even though the mean wind speed is greater than the mean wind at Mykjeneset. This is as expected due to less complex topography in the neighbouring area. Most of the high TKE values at Giskhaugen correspond to strong wind events, i.e. above 12 m/s. Most winds below the strong wind threshold are also below the severe turbulence threshold. Many weak wind cases from the south-west and west are above the severe turbulent threshold. This might be due to the proximity of the location to Astritinden in the west.

Sporra is the location with highest mean TKE and wind speed as can be seen in Figure 4.12c and 4.8, respectively. From the scatterplot, one can observe that most of the strong wind cases from south to west generate high TKE values. From Figure 4.10 one can see that the south-west side of the fjord is close to high mountains in the west. Winds from these directions probably form downslope windstorms which generate mutch turbulence at the location.

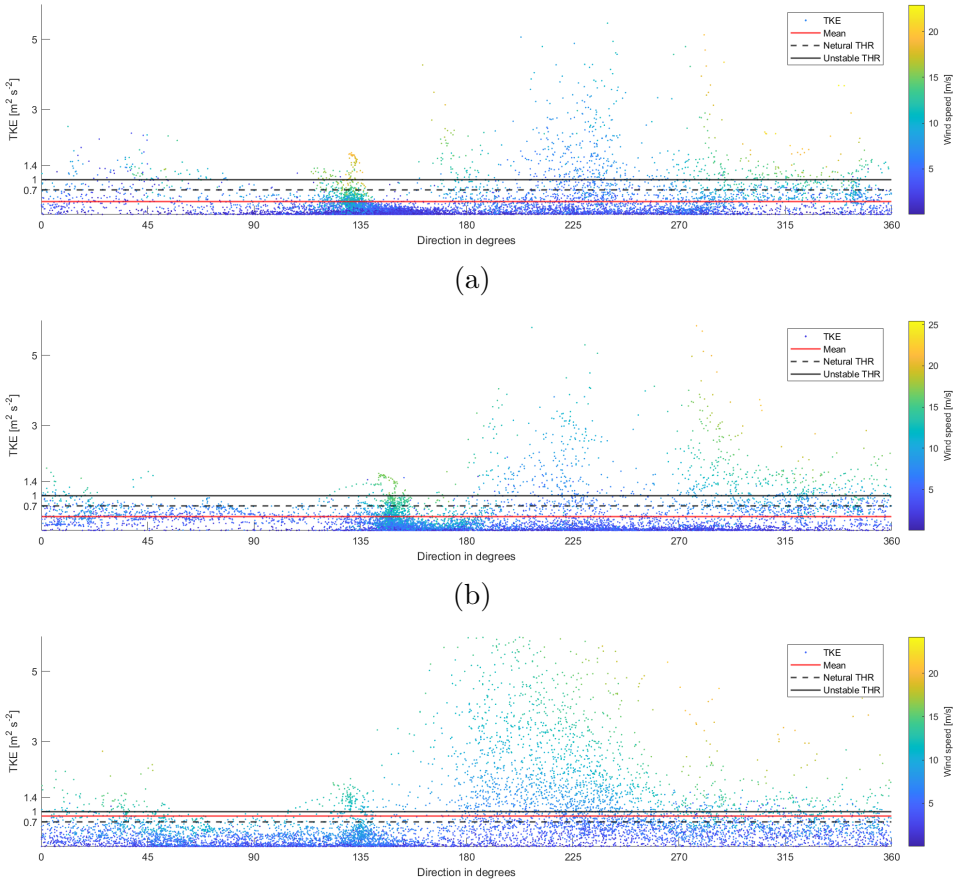

Figure 4.12: Scatter plot of TKE 48 magl, and it's corresponding wind direction, and wind speed at (a) Mykjeneset, (b) Giskhaugen, and (c) Sporra. The solid red line represents the mean TKE at the location. The dashed black line represents the light TKE threshold, and the solid black line represents the moderate TKE threshold. The direction in degrees represents the direction where the wind is blowing from. That means that a wind from 90° are wind from east.

4.6 Power assessment

Figure 4.13 shows normalized histograms for the model predicted wind speeds at each location. The predicted wind speeds from Arome 500 are sorted into 0.4 m/s bins. The solid dashed and dotted red lines represent the energy output from that specific wind speed from 9 September 2019 to 9 September 2020 without any correction for turbulence. Since a full year of wind-speed measurements are used, the annual energy produced from a given turbine $E_{tot,E-XX}$ can be expressed as:

$$E_{tot,E-XX} = \sum_{i=1}^{N} nP_o \tag{4.1}$$

where N is the total number of unique wind speeds, n is the number of events at the unique wind speed, and P_o is the power output corresponding to a wind speed in the histogram which is defined by the power curve shown in Figure 3.8.

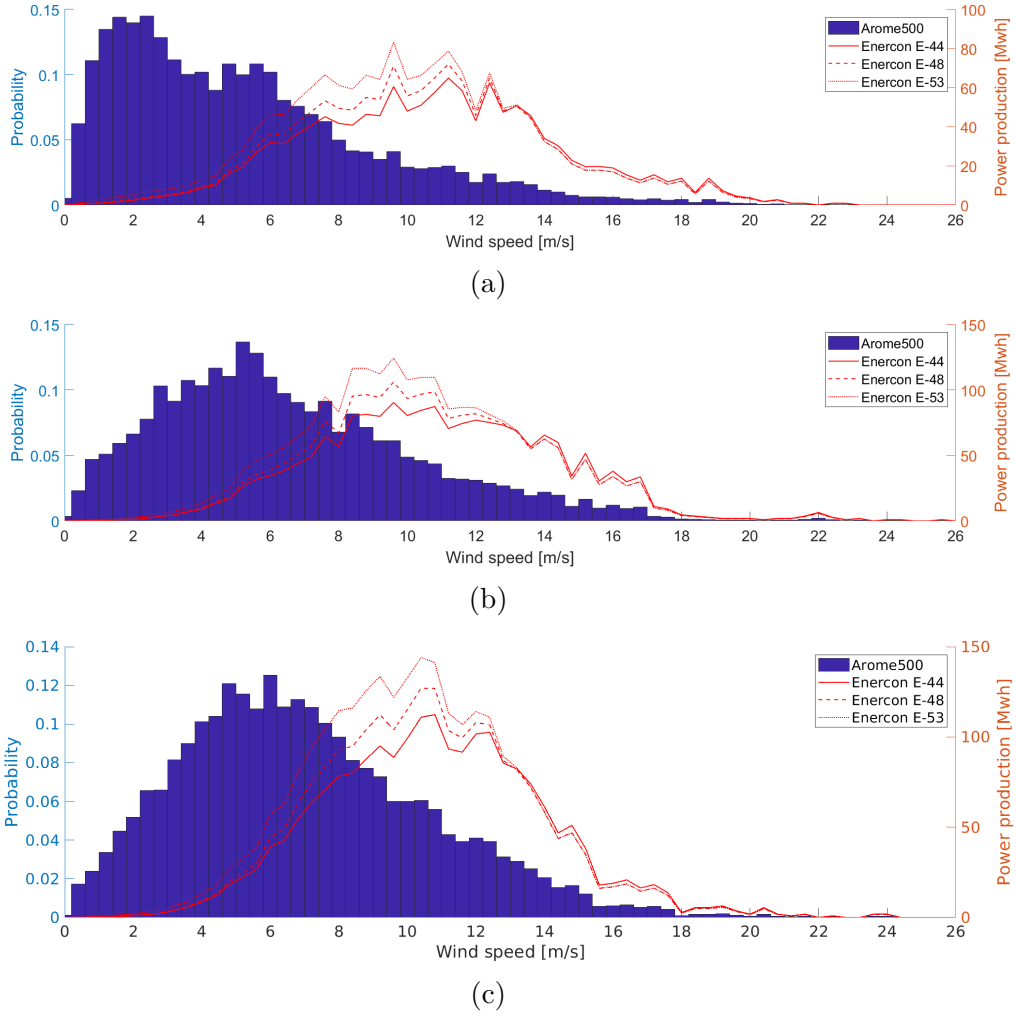

Figure 4.13: Normalized histogram plot of the wind speeds 48 magl obtained from Arome 500 at the three different locations (a) Mykjeneset, (b) Giskhaugen and (c) Sporra. The solid green line represents the fitted Weibull probability function. The solid, dotted and dashed red lines represent the power production in Mwh for the Enercon E-44, Enercon E-48, and Enercon-E53, respectively

Table 4.8 show the annual energy production, the capacity factor, and the power coefficient at each location for all turbines without any turbulence corrections. In calculations of energy in the wind used to calculate the power coefficient, the density is calculated using temperature and pressure 2 magl. However, from the table, one can observe that the annual energy production is largest for the E-53 turbine and smallest for the E-44. This is due to the difference in rotor diameter of the turbines as well as the. The capacity factor also follows this pattern. At Sporra, the highest yearly mean wind speed location, all turbines had a significant higher capacity factor compared to the other locations. Furthermore, the turbine with the highest power

coefficient is the smallest, i.e. the smallest turbine is most efficient in extracting power from the wind.

Location	Windturbine	E_o[MWh]	CF [%]	C_p [%]
Mykjeneset	Enercon E-44	1314	16.6	36.2
	Enercon E-48	1415	20.1	32.7
	Enercon E-53	1620	23	30.7
Giskhaugen	Enercon E-44	1883	23.8	36.5
	Enercon E-48	2026	28.8	33
	Enercon E-53	2301	32.7	30.8
Sporra	Enercon E-44	2099	26.5	38.6
	Enercon E-48	2278	32.4	35.1
	Enercon E-53	2587	36.8	32.7

Table 4.8: Calculations of the annual energy output E_o, capacity factor CF, and the power coefficient C_p without any turbulence corrections for each turbine at all locations.

Furthermore, the output power from a wind turbine is as earlier mentioned, dependent on turbulence. For stronger winds, an underperformance is observed for a winds which correspond to have a TKE above the severe threshold defined in Table 3.3. Thus power outputs are reduced by 18% for observations having severe TKE and winds above 9 m/s. Table 4.9 show the annual energy production, capacity factor and power coefficient after these reductions. From the table, one can observe that the capacity factor and the wind turbines' power coefficients decreases as expected. The smallest turbine had the largest decrease in the power coefficient, whereas the largest turbine had the largest decrease in capacity factor. Furthermore, Sporra had the most significant decrease in annual power production. However, this was expected due to a high mean TKE value.

Location	Windturbine	E_o[MWh]	CF [%]	C_p [%]
Mykjeneset	Enercon E-44	1282	16.2	35.3
	Enercon E-48	1383	19.7	32
	Enercon E-53	1587	22.6	30.1
Giskhaugen	Enercon E-44	1825	23.1	35.4
	Enercon E-48	1971	28	32.1
	Enercon E-53	2244	31.9	30
Sporra	Enercon E-44	1938	24.5	35.6
	Enercon E-48	2113	30	32.6
	Enercon E-53	2413	34.3	30.5

Table 4.9: Calculations of the annual energy output E_o, capacity factor CF, and the power coefficient C_p with turbulence corrections for winds above 9 m/s and for a TKE value above 1.4 m^2/s^2.

Furthermore, additional reductions have been made due to the large reductions seen at Fakken wind farm on Vannøya. Table 4.10 show the annual energy output, capacity factor and power coefficient after applying zero production for winds corresponding

to TKE values above 3.0 m^2/s^2. This shows that Sporra suffers the most from this reduction. Mykjeneset and Giskhaugen show only small differences in annual energy production. Furthermore, the capacity factor decreases most for the E-53 turbine, and the smallest turbine have the largest drop in power coefficient. This may imply that the E-44 turbine is more sensitive to turbulence than the other turbines.

For the turbulent reductions done in Table 4.10, the capacity factor of the biggest E-53 turbine at Mykjeneset is below Giskhaugen and Sporra and far below the annual average capacity factor which was in USA 35 % in 2018. This is a result of the lower mean wind speed at Mykjeneset compared to Sporra and Giskhaugen.

Location	Windturbine	E_o[MWh]	CF [%]	C_p [%]
Mykjeneset	Enercon E-44	1246	15.8	34.3
	Enercon E-48	1346	19.1	31.1
	Enercon E-53	1547	22	29.3
Giskhaugen	Enercon E-44	1760	22.2	34.1
	Enercon E-48	1908	27.1	31.1
	Enercon E-53	2180	31	29.1
Sporra	Enercon E-44	1566	19.8	28.8
	Enercon E-48	1749	24.9	27
	Enercon E-53	2039	29	25.8

Table 4.10: Calculations of the annual energy output E_o, capacity factor CF, and the power coefficient C_p with no production for TKE values above 3.0 m^2/s^2 and a reduction of 18% for wind speeds above 9 m/s that have TKE value above 1.4 m^2/s^2.

Sources of error

Several sources of error in the production estimates have to be taken into account. First of all, the yearly mean wind speed are obtained from model data. From the power in the wind equation defined in Chapter 2, Section 2.3, one can see that the power in the wind varies as the cube of the wind speed; large errors in predicted wind speed by the model would lead to large errors in the production estimates. The Arome 500 model used here had low MBE and MAE for both Senjahopen and Hekkingen, which is close to Mykjeneset and Giskhaugen, respectively. However, even though the distances are short, large wind speed variations can occur due to the complex terrain. Thus the model performance may not necessarily be accurate at other locations nearby the verified locations. In addition to speed errors, the power output from the turbine is calculated by the manufacturer by using a standard air density of $\rho_0 = 1.225$ kg/m^3. No corrections are done for the variations in air density, which also may result in errors. However, compared to the errors due to fluctuations in wind speed, these are small as is evident from the power in the wind equation.

Furthermore, whether or not the reductions due to turbulence reduces the annual energy production enough or too much is questionable. Several error sources arise such as if the TKE divisions are correctly set and the reduction values according to

these, and if the turbulent kinetic energy predicted by the model is correct. However, observations are needed to give more accurate estimates of the turbulence and finally, more accurate production estimates.

Chapter 5

Conclusion and further work

5.1 Conclusion

The three LAM Arome 500, AROME-Arctic and NORA3 with high horizontal resolutions of 0.5, 2.5 and 3.0 km have been investigated over northern Senja. The models are compared against observations at the three observation sites; Innhesten, Senjahopen and Hekkingen. No correction factor were found between NORA3 and Arome 500. At Hekkingen, the NORA3 dataset showed large errors in 50 magl wind. At Senjahopen both the NORA3 dataset and Arome 500 dataset covered less than a year. Thus a correlation between the models at these locations was not obtained. At Innhesten, NORA3 performed better than the Arome 500 model. Arome 500 showed the best model results for flow in the fjords and in the less complex area at Hekkingen. The gap winds and the downslope windstorms was best resolved by Arome 500 which was especially evident in Mefjorden during the strong wind event 15. September 2019. The Arome 500 model was, therefore, the only model used in the wind resource assessment since only areas in the fjords and close to sea level was investigated.

From the map of annual mean wind speed from Arome 500, it was evident that higher wind speeds with low TKE were observed in the outermost parts of the fjords. Wind resources at three locations where investigated; Sporra, Mykjeneset and Giskhaugen. These were chosen due to a high yearly mean wind speed and low mean TKE, proximity to existing road and grid lines, and the neighbouring area around some of the biggest power consumers at northern Senja. Annual energy production estimates from these locations were produced using power curves from the three Enercon turbines with rated power below 1 MW; E-44, E-48, and E-53.

The E-53 turbine had the highest annual energy production of 1620, 2301 and 2587 MWh at Mykjeneset, Giskhaugen, and Sporra. The E-53 turbine had the highest CF of 23, 32.7, and 36,8 % whereas the E-44 turbine had the highest power coefficient of 36.2, 36.5, and 38.6 % at Mykjeneset, Giskhaugen and Sporra, respectively. A lower annual mean wind speed at Mykjeneset is the reason for a lower capacity factor and annual production at the location compared to the other two.

Due to the complexity of the surrounding terrain around the locations turbulence was investigated and corrected for. This was done in order to give more accurate production estimates as turbulence can reduce the power output from the turbines. The Sporra location had the most reductions in annual energy production due to the turbulence corrections. The E-44 turbine showed at all locations the largest decrease in power coefficient, whereas the E-53 turbine showed the largest decrease in capacity factor. Only small differences in annual energy production was seen at Giskhaugen and Mykjeneset before and after the turbulence corrections. Giskhaugen showed the highest annual production of 2180 MWh and a CF of 31% for the E-53 turbine after the TKE corrections.

5.2 Further work

Several improvements can be made in order to obtain more accurate power assessments and better understanding of the models at northern Senja. Some of them are listed below:

- The model TKE values were not verified against observations in this thesis, thus the TKE probably deviate from the different locations' actual TKE values. It would have been interesting to see the model's performance in similar locations where observed TKE also was available.
- The models could have been set up at Fakken to determine a more accurate TKE categorization and reductions accordingly to this.
- A varying air density was not accounted for when calculating the annual energy output. Differences in humidity and temperature would probably have resulted in a change in the energy output, especially in the winter due to a high air density.
- Initialize the Arome 500 model such that the overlapping periods between all datasets were a minimum of a year to obtain a longer and more accurate comparison between the models. Thus find a scaling factor between the model with the best accuracy in the complex terrain and the model stretching the longest period such that the annual energy production can be estimated with small errors over several years.
- Further investigate Sporra due to proximity to road and power lines. In addition, Skaland mine are located here driven by Skaland Graphite AS.

Appendices

Appendix A: Wind roses Hekkingen

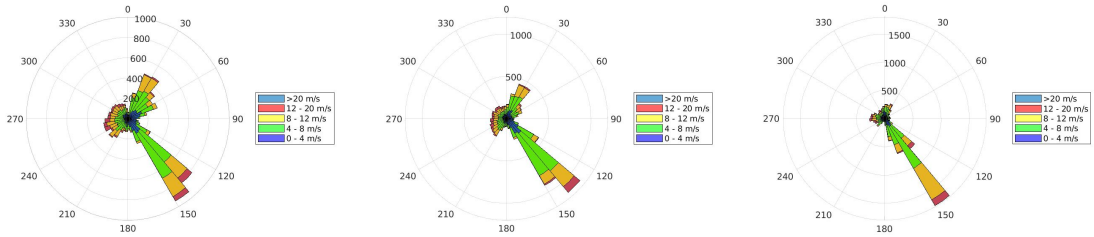

(a) NORA3 (b) AROME-Arctic (c) Observations

Figure A.1: All winds NORA3 and AROME-Arcitc.

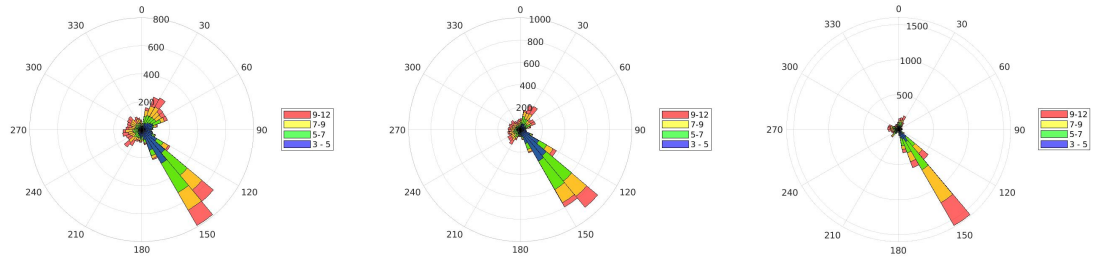

(a) NORA3 (b) AROME-Arctic (c) Observations

Figure A.2: Weak winds NORA3 and AROME-Arcitc.

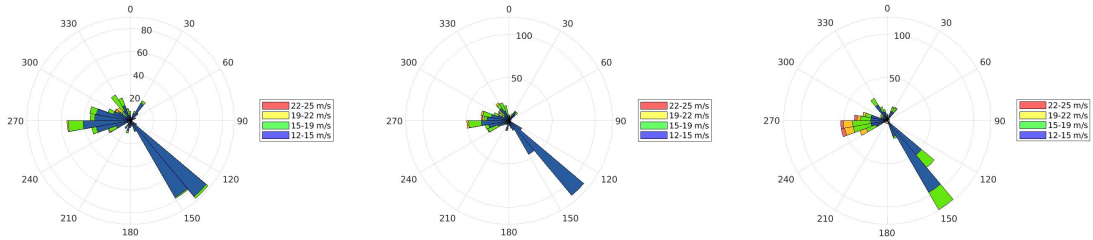

(a) NORA3 (b) AROME-Arctic (c) Observations

Figure A.3: Strong winds NORA3 and AROME-Arcitc.

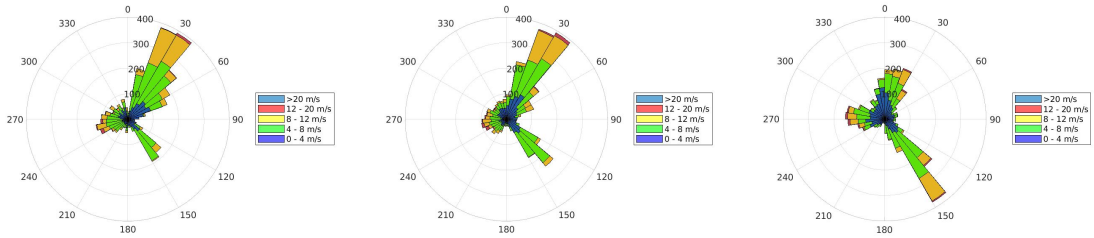

(a) NORA3 (b) AROME-Arctic (c) Observations

Figure A.4: Winds in the summer period for NORA3 and AROME-Arcitc.

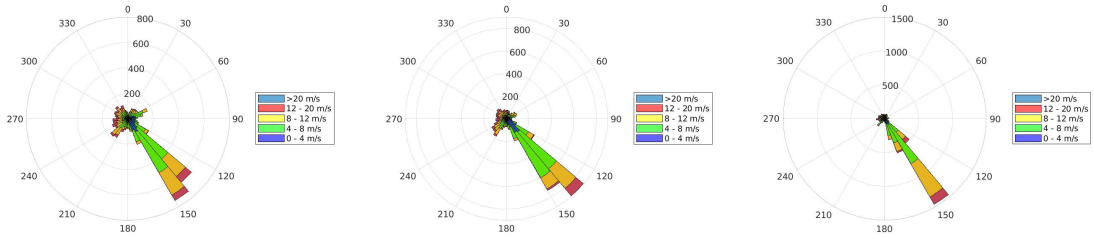

(a) NORA3 (b) AROME-Arctic (c) Observations

Figure A.5: Winds in the winter period for NORA3 and AROME-Arcitc.

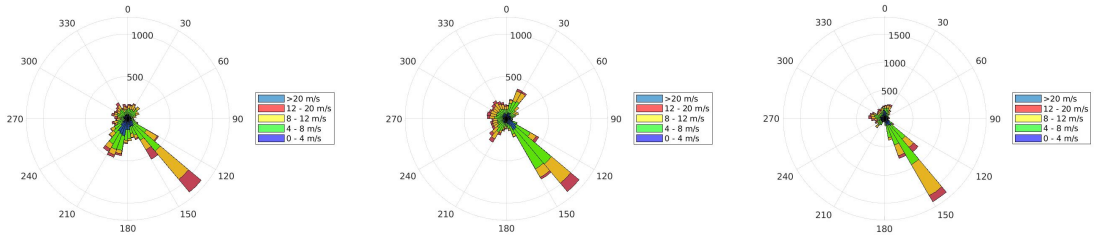

(a) Arome 500 (b) AROME-Arctic (c) Observations

Figure A.6: All winds for Arome 500 and AROME-Arcitc

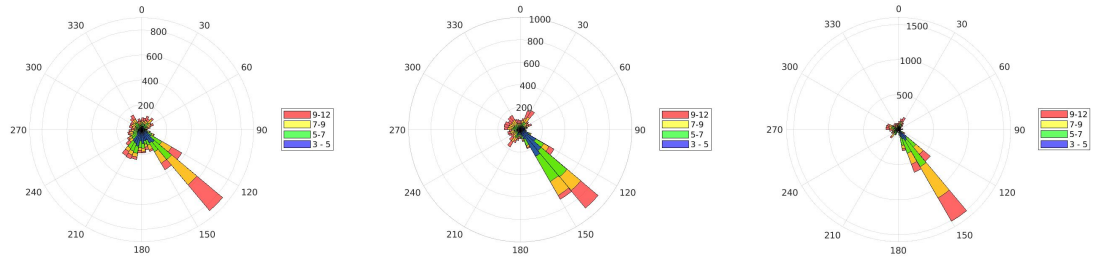

(a) Arome 500 (b) AROME-Arctic (c) Observations

Figure A.7: Weak winds for Arome 500 and AROME-Arcitc

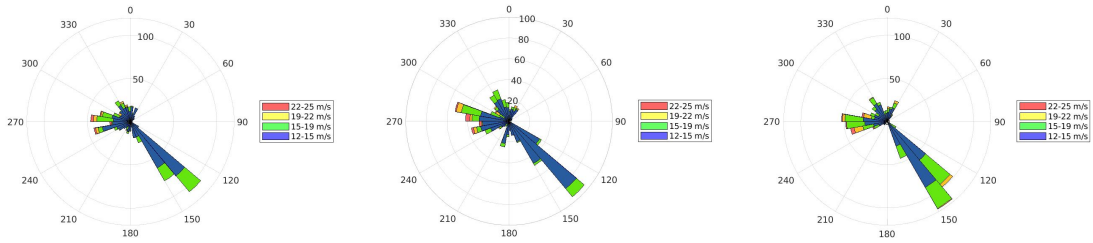

(a) Arome 500 (b) AROME-Arctic (c) Observations

Figure A.8: Strong winds for Arome 500 and AROME-Arcitc

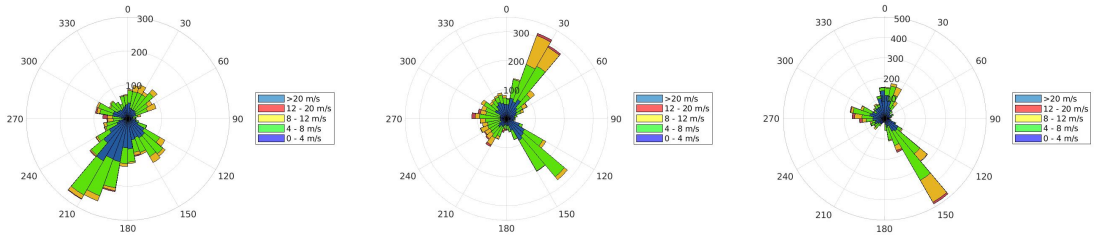

(a) Arome 500 (b) AROME-Arctic (c) Observations

Figure A.9: Windst in the winter period for Arome 500 and AROME-Arcitc

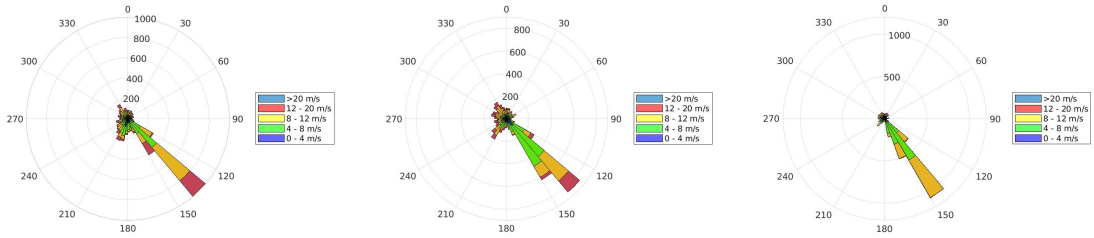

(a) Arome 500 (b) AROME-Arctic (c) Observations

Figure A.10: Winds in the winter period for Arome 500 and AROME-Arcitc

Appendix B: Wind roses Senjahopen

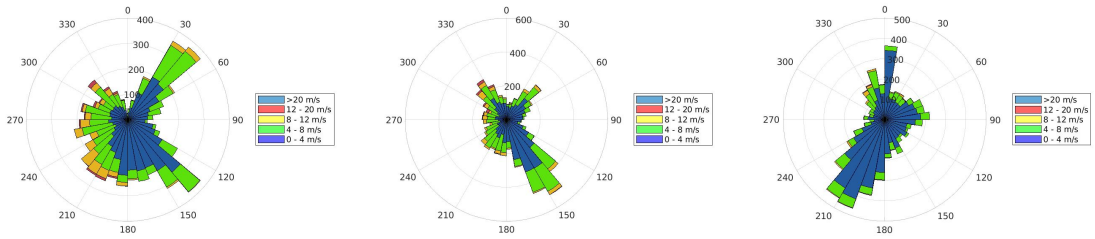

(a) NORA3 (b) AROME-Arctic (c) Observations

Figure B.1: All winds NORA3 and AROME-Arcitc

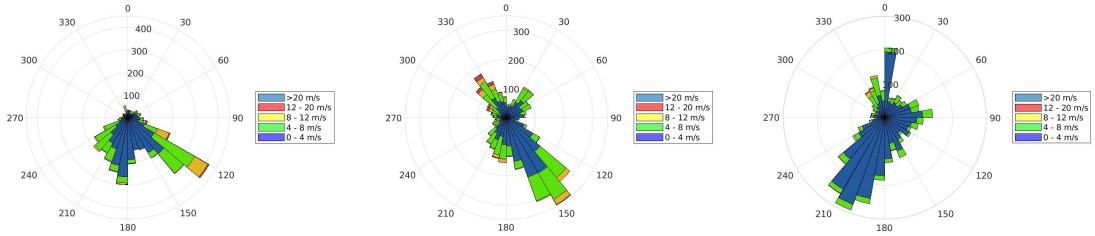

(a) Arome 500 (b) AROME-Arctic (c) Observations

Figure B.2: All winds Arome 500 and AROME-Arcitc

Appendix C: Wind roses Innhesten

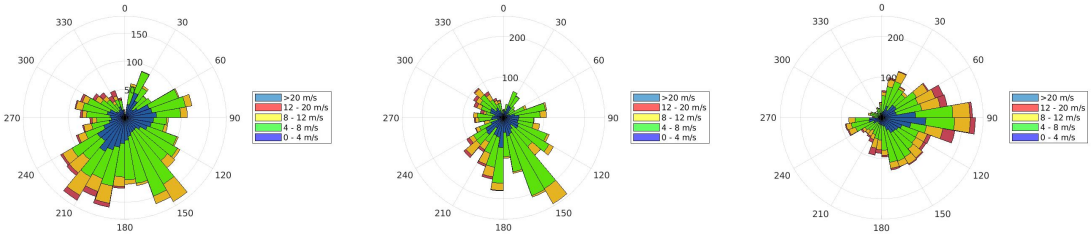

(a) NORA3 (b) AROME-Arctic (c) Observations

Figure C.1: All wind speeds NORA3 and AROME-Arcitc

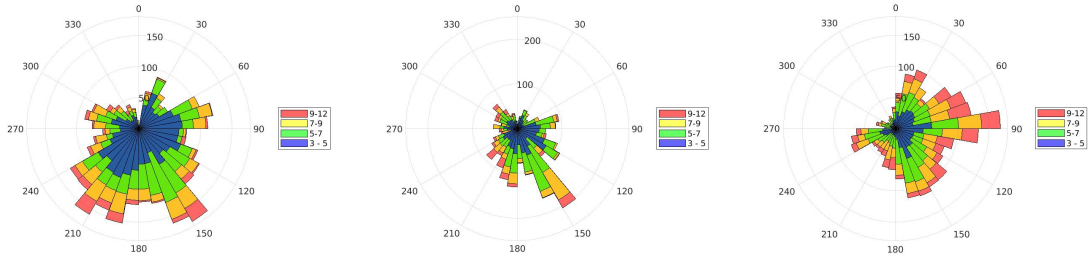

(a) NORA3 (b) AROME-Arctic (c) Observations

Figure C.2: weak winds NORA3 and AROME-Arcitc

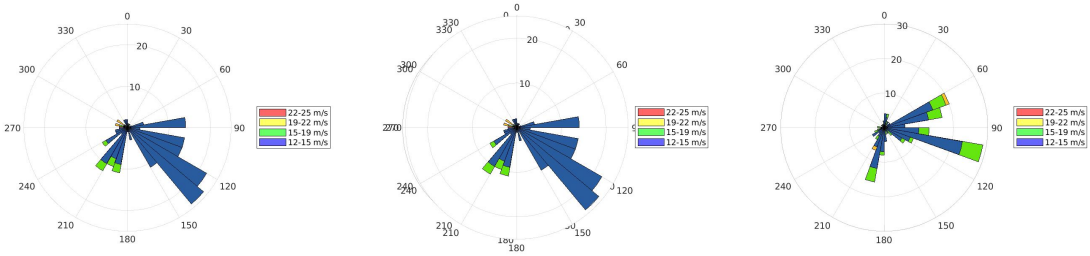

(a) NORA3 (b) AROME-Arctic (c) Observations

Figure C.3: Strong wind speeds NORA3 and AROME-Arcitc

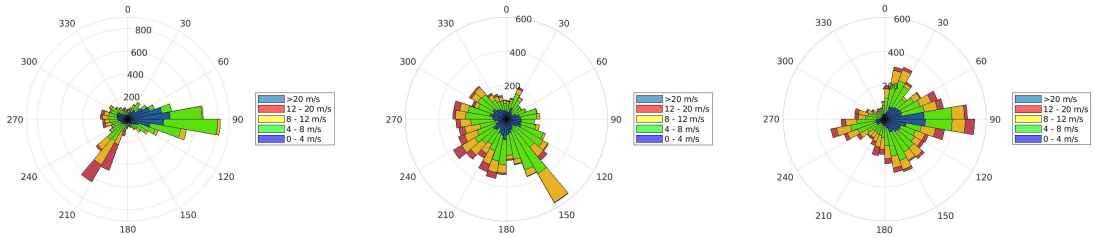

(a) Arome 500 (b) AROME-Arctic (c) Observations

Figure C.4: All wind speeds Arome 500 and AROME-Arcitc

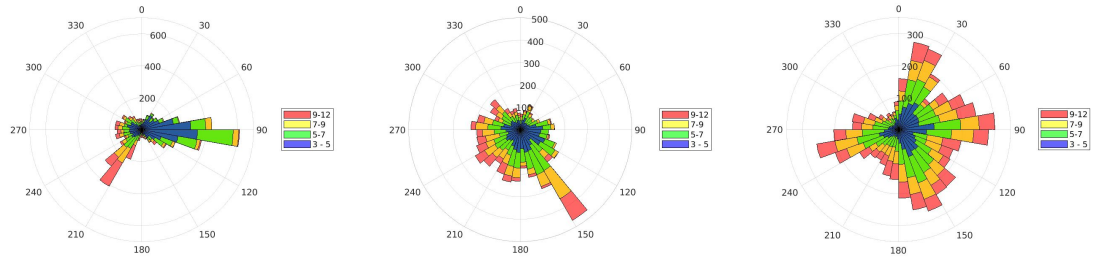

(a) Arome 500 (b) AROME-Arctic (c) Observations

Figure C.5: Weak winds Arome 500 and AROME-Arcitc

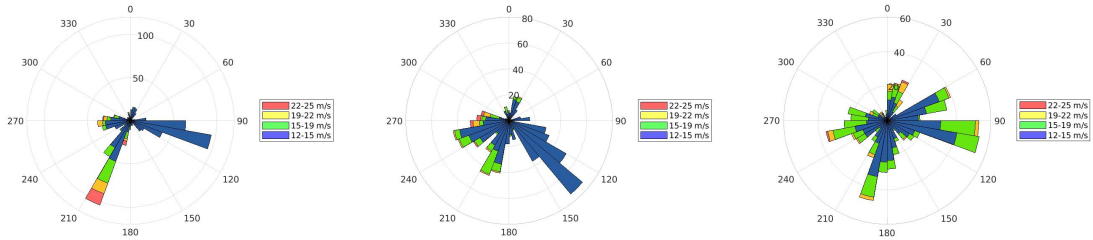

(a) Arome 500 (b) AROME-Arctic (c) Observations

Figure C.6: Strong winds speeds Arome 500 and AROME-Arcitc

Bibliography

1. Ucar, A. & Balo, F. Evaluation of wind energy potential and electricity generation at six locations in Turkey. *Applied Energy* **86,** 1864–1872 (2009).
2. Dorvlo, A. & Ampratwum, D. Wind energy potential for Oman. *Renewable Energy* **26,** 333–338 (2002).
3. Song, M., Chen, K., He, Z. & Zhang, X. Wind resource assessment on complex terrain based on observations of a single anemometer. *Journal of Wind Engineering and Industrial Aerodynamics* **125,** 22–29 (2014).
4. Carta, J. A., Velázquez, S. & Cabrera, P. A review of measure-correlate-predict (MCP) methods used to estimate long-term wind characteristics at a target site. *Renewable and Sustainable Energy Reviews* **27,** 362–400 (2013).
5. Abrahamsen, M., Birkelund, Y., *et al. Coastal wind from satellite measurements and meteorological models for offshore wind power prediction* in *The Twenty-fifth International Ocean and Polar Engineering Conference* (2015).
6. Al-Yahyai, S., Charabi, Y. & Gastli, A. Review of the use of numerical weather prediction (NWP) models for wind energy assessment. *Renewable and Sustainable Energy Reviews* **14,** 3192–3198 (2010).
7. Rontu, L. A study on parametrization of orography-related momentum fluxes in a synoptic-scale NWP model. *Tellus A: Dynamic Meteorology and Oceanography* **58,** 69–81 (2006).
8. Beljaars, A. C., Brown, A. R. & Wood, N. A new parametrization of turbulent orographic form drag. *Quarterly Journal of the Royal Meteorological Society* **130,** 1327–1347 (2004).
9. Kalverla, P., Steeneveld, G.-J., Ronda, R. & Holtslag, A. A. Evaluation of three mainstream numerical weather prediction models with observations from meteorological mast IJmuiden at the North Sea. *Wind Energy* **22,** 34–48 (2019).
10. Vallis, G. K. in *Atmospheric and Oceanic Fluid Dynamics: Fundamentals and Large-Scale Circulation* 2nd ed., 3–54 (Cambridge University Press, 2017).
11. Holton, J. R. & Hakim, G. J. in *An Introduction to Dynamic Meteorology (Fifth Edition)* (eds Holton, J. R. & Hakim, G. J.) Fifth Edition, 31–66 (Academic Press, Boston, 2013). ISBN: 978-0-12-384866-6. `http://www.sciencedirect.com/science/article/pii/B9780123848666000027`.
12. Abbe, C. The physical basis of long-range weather forecasts. *Monthly Weather Review* **29,** 551–561 (1901).

13. Bjerknes, V. Das Problem der Wettervorhers-age, betrachtet vom Standpunkte der Mechanik und der Physik. *Meteor. Z.* **21,** 1–7 (1904).

14. Richardson, L. F. *Weather prediction by numerical process* (Cambridge university press, 2007).

15. Huang, X.-Y. & Vedel, H. An introduction to data assimilation (Mar. 2002).

16. Landberg, L. *Meteorology for wind energy: an introduction* (John Wiley & Sons, 2015).

17. Mesinger, F. & Arakawa, A. Numerical methods used in atmospheric models (1976).

18. Hortal, M. & Simmons, A. Use of reduced Gaussian grids in spectral models. *Monthly Weather Review* **119,** 1057–1074 (1991).

19. Phillips, N. A. A coordinate system having some special advantages for numerical forecasting. *Journal of Meteorology* **14,** 184–185 (1957).

20. Simmons, A. J. & Burridge, D. M. An energy and angular-momentum conserving vertical finite-difference scheme and hybrid vertical coordinates. *Monthly Weather Review* **109,** 758–766 (1981).

21. Jeppesen, J. *Fact sheet: ECMWF's use of satellite observations* Sept. 2020. https://www.ecmwf.int/en/about/media-centre/focus/2020/fact-sheet-ecmwfs-use-satellite-observations#:~:text=Satellite%20observations%20make%20a%20crucial,provided%20by%20in%20situ%20measurements..

22. Randriamampianina, R. & Storto, A. Aladin-HARMONIE/Norway and its assimilation system—The implementation phase. *HIRLAM Newsletter* **54,** 20–30 (2008).

23. Durran, D. R. in *Numerical Methods for Fluid Dynamics* 357–391 (Springer, 2010).

24. Diamantakis, M. *The semi-Lagrangian technique in atmospheric modelling: current status and future challenges* in *ECMWF Seminar in numerical methods for atmosphere and ocean modelling* (2013), 183–200.

25. Ulazia, A., Nafarrate, A., Ibarra-Berastegi, G., Sáenz, J. & Carreno-Madinabeitia, S. The consequences of air density variations over Northeastern Scotland for offshore wind energy potential. *Energies* **12,** 2635 (2019).

26. Kalmikov, A. in *Wind Energy Engineering* 17–24 (Elsevier, 2017).

27. Wiser, R. H. & Bolinger, M. 2018 Wind Technologies Market Report (2019).

28. Stull, R. B. *An introduction to boundary layer meteorology* (Springer Science & Business Media, 2012).

29. Herr, D. & Heidenreich, D. How turbulent winds abuse wind turbine drivetrains. *Wind Power Engineering* (2015).

30. Sumner, J. & Masson, C. Influence of atmospheric stability on wind turbine power performance curves (2006).

31. St Martin, C. M., Lundquist, J. K., Clifton, A., Poulos, G. S. & Schreck, S. J. Wind turbine power production and annual energy production depend on atmospheric stability and turbulence. *Wind Energy Science (Online)* **1** (2016).

32. Emeis, S. *Wind energy meteorology: atmospheric physics for wind power generation* (Springer, 2018).

33. Weber, R. O. & Kaufmann, P. Relationship of synoptic winds and complex terrain flows during the MISTRAL field experiment. *Journal of Applied Meteorology* **37,** 1486–1496 (1998).

34. Whiteman, C. D. & Doran, J. C. The relationship between overlying synoptic-scale flows and winds within a valley. *Journal of Applied Meteorology* **32,** 1669–1682 (1993).

35. Smith, R. B. On severe downslope winds. *Journal of the atmospheric sciences* **42,** 2597–2603 (1985).

36. Bengtsson, L. *et al.* The HARMONIE–AROME model configuration in the ALADIN–HIRLAM NWP system. *Monthly Weather Review* **145,** 1919–1935 (2017).

37. Bénard, P. *et al.* Dynamical kernel of the Aladin–NH spectral limited-area model: Revised formulation and sensitivity experiments. *Quarterly Journal of the Royal Meteorological Society: A journal of the atmospheric sciences, applied meteorology and physical oceanography* **136,** 155–169 (2010).

38. Davies, H. A lateral boundary formulation for multi-level prediction models. *Quarterly Journal of the Royal Meteorological Society* **102,** 405–418 (1976).

39. Seity, Y. *et al.* The AROME-France convective-scale operational model. *Monthly Weather Review* **139,** 976–991 (2011).

40. Joseph, J. H., Wiscombe, W. & Weinman, J. The delta-Eddington approximation for radiative flux transfer. *Journal of the Atmospheric Sciences* **33,** 2452–2459 (1976).

41. Fouquart, Y. *et al.* Computations of solar heating of the Earth's atmosphere: A new parameterization (1980).

42. Lascaux, F., Richard, E. & Pinty, J.-P. Numerical simulations of three different MAP IOPs and the associated microphysical processes. *Quarterly Journal of the Royal Meteorological Society: A journal of the atmospheric sciences, applied meteorology and physical oceanography* **132,** 1907–1926 (2006).

43. Bouteloup, Y., Seity, Y. & Bazile, E. Description of the sedimentation scheme used operationally in all Météo-France NWP models. *Tellus A: Dynamic Meteorology and Oceanography* **63,** 300–311 (2011).

44. Lenderink, G. & Holtslag, A. A. An updated length-scale formulation for turbulent mixing in clear and cloudy boundary layers. *Quarterly Journal of the Royal Meteorological Society: A journal of the atmospheric sciences, applied meteorology and physical oceanography* **130,** 3405–3427 (2004).

45. De Rooy, W. C. & Pier Siebesma, A. Analytical expressions for entrainment and detrainment in cumulus convection. *Quarterly Journal of the Royal Meteorological Society* **136,** 1216–1227 (2010).

46. De Rooy, W. C. *et al.* Entrainment and detrainment in cumulus convection: An overview. *Quarterly Journal of the Royal Meteorological Society* **139,** 1–19 (2013).

47. Le Moigne, P. *et al.* SURFEX scientific documentation. *Note de centre (CNRM/GMME), Météo-France, Toulouse, France* (2009).

48. *wiki.met.no* `https://wiki.met.no/fimex/start`.

49. Scott, D. W. in, 79–131 (John Wiley & Sons, 2020).

50. Willmott, C. J. & Matsuura, K. Advantages of the mean absolute error (MAE) over the root mean square error (RMSE) in assessing average model performance. *Climate research* **30,** 79–82 (2005).

51. Muljadi, E., Butterfield, C. S. & Buhl Jr, M. L. EFFECTS OF TURB POWER GENERATIO R VARIABLE-SPEED TURBINES.

52. Jacobsen, M. *Short-term wind power prediction based on Markov chain and numerical weather prediction models: A case study of Fakken wind farm* MA thesis (UiT The Arctic University of Norway, 2014).